CONTINUOUS NANOPARTICLE SIZING AND CHARACTERIZATION VIA MICROFLUIDICS

A Thesis

by

FANXU MENG

Submitted to the Office of Graduate and Professional Studies of
Texas A&M University
in partial fulfillment of the requirements for the degree of

DOCTOR OF PHILOSOPHY

Chair of Committee,	Victor Ugaz
Committee Members,	Zhengdong Cheng
	Yassin Hassan
	Arul Jayaraman
Head of Department,	M. Nazmul Karim

May 2015

Major Subject: Chemical Engineering

ABSTRACT

High-throughput manufacturing of nanomaterial-based products demands robust online characterization and quality control tools capable of continuously probing the in suspension state. But existing analytical techniques are challenging to deploy in production settings because they are primarily geared toward small-batch ex-situ operation in research laboratory environments. Here we introduce an approach that overcomes these limitations by exploiting surface complexation interactions that emerge when a micron-scale chemical discontinuity is established between suspended nanoparticles and a molecular tracer. The resulting fluorescence signature is easily detectable and embeds surprisingly rich information about composition, quantity, size, and morphology of nanoparticles in suspension independent of their agglomeration state. We show how this method can be straightforwardly applied to enable continuous sizing of commercial ZnO nanoparticles, and to instantaneously quantify the anatase and rutile composition of multi-component TiO_2 nanoparticle mixtures pertinent to photo catalysis and solar energy conversion. A transport model of the interfacial complexation process is formulated to qualitatively confirm the experimental discovery and to provide understanding of the transport and binding processes.

Practical utility is demonstrated by combining our detection method with a cyclone sampler to enable continuous monitoring of airborne nanoparticles. Our method uniquely combines ultra-high flow rate sampling (up to thousands of liters per minute) with sensitive detection based on localized fluorescent complexation, permitting rapid

quantitative measurement of airborne nanoparticle concentration. By coupling these components, we show initial results demonstrating detection of airborne ultrafine Al_2O_3 nanoparticles at environmental concentrations below 200 μg m^{-3} in air sampled at 200 L min^{-1}. This capability suggests potential for online monitoring, making it possible to establish dynamic exposure profiles not readily obtainable using current-generation personal sampling instruments. The underlying fluorescent complexation interactions are inherently size and composition dependent, offering potential to straightforwardly obtain continuous detailed characterization.

The increasing commercial prevalence of nanoparticle-based materials also introduces a new demand for robust online characterization tools amenable toward online monitoring in manufacturing settings. We address this need by showing how electrical conductivity measurements can be exploited to instantaneously obtain size and species information in oxide nanoparticle suspensions. This approach is readily implemented in an easy to build platform that can be employed either online to provide real-time feedback during continuous synthesis and processing, or offline for evaluation of test samples obtained from larger batches. Our implementation enables accurate results to be obtained using inexpensive digital multimeters, suggesting broad potential for on-site deployment in industrial settings.

ACKNOWLEDGEMENTS

I would like to thank my committee chair, Dr. Victor Ugaz, for introducing me to work in these interesting projects and for enlighteningly discussing to help me to find the right approaches. I am greatly thankful for your generous support in both my academic and personal life. And thanks my committee members, Dr. Zhengdong Cheng, Dr. Yassin Hassan and Dr. Arul Jayaraman, for their guidance and support throughout this research.

Thanks to my mother and father for their encouragement, patience and love. Thanks also go to my friends, lab mates and the department faculties and staffs for making my time at Texas A&M University a great experience.

TABLE OF CONTENTS

Page

LIST OF FIGURES

Page

LIST OF TABLES

Page

CHAPTER I

INTRODUCTION AND LITERATURE REVIEW[*]

The Nanomaterial Characterization Bottleneck between Scientific Discovery and Commercialization

Nanomaterials have long functioned as key additives in a broad array of familiar products (e.g., paints, sunscreens, composites), but their significance has grown considerably in recent years as their exceptional electrical, optical, and mechanical properties become harnessed in sophisticated new ways (e.g., photovoltaic, catalysis, sensors (Fujishima, Zhang, & Tryk, 2008; Funk, Hokkanen, Burghaus, Ghicov, & Schmuki, 2007; Hardin, Snaith, & McGehee, 2012; M. Li, Schnablegger, & Mann, 1999; G. Z. Liu et al., 2012; Mao & Wong, 2006; Shklover et al., 1997)). Many of these applications involve processing of suspension-based nanomaterials and demand precise control over properties such as chemistry, size, morphology and/or crystalline structure (e.g. anatase vs. rutile) (Fujishima et al., 2008; Mao & Wong, 2006; Ohno, Sarukawa, Tokieda, & Matsumura, 2001; Pileni, 2003; Satoh, Nakashima, Kamikura, & Yamamoto, 2008). Unfortunately, characterization methods have generally failed to keep up with the rapid pace of material discovery. Measurement approaches such as dynamic light scattering (DLS) and electron microscopy (SEM, TEM)—workhorses in the field for decades—are challenging to employ outside of research-oriented laboratory settings and

[*] Reprinted with permission from "Localized Fluorescent Complexation Enables Rapid Monitoring of Airborne Nanoparticles", F. Meng, M. D. King, Y. A. Hassan and V. Ugaz, 2014, *Environmental Science: Nano*, 358-366, Copyright 2014 by Royal Society of Chemistry.

do not easily lend themselves to continuous analysis because of their sample requirements (dry powder, dilution), operating conditions (high vacuum), and measurement duration (tens of minutes). Sizing results are also often sensitive to the presence of agglomerates and aggregates of primary particles. This lack of continuous characterization tools scalable toward online deployment, particularly methods capable of directly probing the in-suspension state to simultaneously obtain size and species information (e.g., to support continuous nanomaterial synthesis (deMello, 2006; Dendukuri & Doyle, 2009; Dendukuri, Pregibon, Collins, Hatton, & Doyle, 2006; Duraiswamy & Khan, 2010; Kenis, Ismagilov, & Whitesides, 1999; Khan & Jensen, 2007; Rahman et al., 2013; H. Z. Wang, Nakamura, Uehara, Miyazaki, & Maeda, 2002)), has made it challenging to establish standardized manufacturing-scale quality control benchmarks and therefore imposes a significant bottleneck between scientific discovery and commercialization (Richman & Hutchison, 2009).

Environmental Monitoring of Airborne Nanoparticle

Nanoparticle safety, particularly in occupational settings, has also become a timely topic of intense interest. Increased environmental exposure is an unavoidable consequence of the growing prevalence of nanomaterials, posing new and largely unknown risks to human health (Balbus et al., 2007; Bonner et al., 2013; Borm et al., 2000; Hext, Tomenson, & Thompson, 2005; Karakoti, Hench, & Seal, 2006; Trouiller, Reliene, Westbrook, Solaimani, & Schiestl, 2009; J. J. Wang, Sanderson, & Wang, 2007). Efforts to assess safe exposure limits and establish correlations with potentially adverse health consequences critically depend on the ability to monitor the concentration

of airborne nanomaterials (Nazarenko, Lioy, & Mainelis, 2014; O'Shaughnessy, 2013). Several commercially available techniques such as the Fast Mobility Particle Sizer (FMPS) (Jeong & Evans, 2009; B. P. Lee, Li, Flagan, Lo, & Chan, 2013) and TSI NanoScan (Tritscher et al., 2013) have recently emerged, which enable continuous, albeit unspecific, monitoring of airborne nanomaterials. However the majority of existing collection and monitoring technologies do not permit simultaneous continuous sampling and characterization because analysis is predominantly performed offline at a later time using a different instrumentation. Existing samplers and particle counters are limited by their ability to access only relatively low air inflow rates (below ~30 L min^{-1}) (Hong et al., 2009; Khlystov, Wyers, & Slanina, 1995; Orsini et al., 2003; Williams, Goldstein, Kreisberg, & Hering, 2006) resulting in a paradigm based on deploying "personal" sampling devices to interrogate small volumes at a few representative locations within the global environment of interest (Cena, Anthony, & Peters, 2011; Tsai et al., 2012; Zhou, Irshad, Tsai, Hung, & Cheng, 2013). However, this strategy is inherently slow (continuous sampling must be performed over one or more full workdays to collect sufficient materials for analysis) and excludes the majority of the workspace air volume (introducing the possibility that hazardous exposure levels may be encountered over timescales below those accessible to the sampler) (Holder, Vejerano, Zhou, & Marr, 2013; Vejerano, Leon, Holder, & Marr, 2014). Efforts have been made to measure spatial concentrations at the manufacturing plant scale (Batterman et al., 1998; Evans, Heitbrink, Slavin, & Peters, 2008; Heitbrink et al., 2009), but considerable timescales are required to collect these data, and they may be subject to spatial

variability. Additional considerations emerge in terms of detection. Here, a wide range of characterization tools are available that provide sensitive analysis of collected nanoparticles (e.g., scanning mobility particle sizers (SMPS), ion chromatography, mass spectrometry (MS), and electron microscopy (EM) (Justino, Rocha-Santos, & Duarte, 2011; Morawska et al., 2009; Orsini et al., 2003; Sotiriou et al., 2014)). But many of these methods, particularly MS and EM-based techniques, function optimally in a dedicated laboratory setting (Sadik et al., 2009) and can be challenging to adapt for online use.

The current inability to perform dynamic studies has recently been pointed out by both the US National Academy of Sciences (US National Academy of Sciences, 2012) and the European Commission Joint Research Centre (The Joint Research Centre of the European Commission, 2012) as an area where integrated approaches amenable to online monitoring are needed. Both of these reports cite limitations in current-generation samplers that, while useful in providing coarse-scale assessments of post-inhalation contact, are unable to provide a time-resolved picture of the transport and fate of dispersed nanomaterials. The resulting lack of data pertinent to dispersal dynamics has made it challenging to develop realistic exposure models that extend beyond elementary respiratory pathways. These gaps are emerging at a time when recent toxicological studies involving nanomaterials previously considered benign are calling previously accepted exposure standards into question (Liou et al., 2012; Weir, Westerhoff, Fabricius, Hristovski, & von Goetz, 2012). Even when high-volume nanoparticle sampling has been demonstrated, analysis is performed using conventional inertial filter-

based methods that are not readily scalable toward continuous monitoring (Hata et al., 2013). A need therefore exists for integrated approaches capable of (1) continuously sampling a broad range or air volumes encountered in realistic workspace environments and (2) performing online detection and analysis of the collected nanoparticles.

Objectives and Outlines

Here we introduce a family of approaches that overcome limitations of conventional small-batch analytical methods, enabling continuous online quantification and characterization of nanoparticle composition, size, and morphology, directly in suspension and independent of agglomeration state. Our methods are based on exploiting surface complexation interactions that emerge when a sharp (micron-scale) chemical discontinuity is established between suspended nanoparticles and a molecular tracer in a laminar flow environment that removes limitations associated with convective transport and mixing (Figure 1a).

In Chapter II, we describe the experimental techniques employed, such as reagents, devices, and operational protocols. There is also brief introduction about the computational modeling and simulation methods we have applied.

In Chapter III, we show how the easily detectable interfacial fluorescence signature embeds surprisingly rich information about particle species (via the nature of fluorescence enhancement or quenching), size (via the relative magnitude of the fluorescence signature), and their combined concentration dependence. The extent of fluorescence enhancement/quenching and lateral shift of the interface between co-flowing nanoparticle and tracer streams are observables that, when supplied as inputs to

a physico-chemical model we have developed, make it possible to instantly obtain physical parameters associated with the suspended nanomaterials from a single convenient in-situ snapshot measurement (Figure 1b).

In Chapter IV, we couple the proven high flow rate air sampling capacity of a wetted wall cyclone (WWC) collector incorporating a low cutpoint slot geometry specifically optimized for nanoparticle collection (up to > 1000 L min^{-1}) (Hu & McFarland, 2007; McFarland et al., 2010) with a continuous-flow microfluidic component that provides online detection capability (Figure 2a). The characteristic flow rate of the fluidic output from the WWC (0.04–0.2 mL min^{-1}) closely matches the flow rates imposed for characterization of interfacial fluorescence, thereby introducing the possibility of enabling continuous detection by directly coupling both components. Since the local interfacial intensity profile sensitively depends on the quantity of suspended nanoparticles, the corresponding environmental concentration can be straightforwardly inferred (Figure 2b).

In Chapter V, we seek to leverage the inherent simplicity of DC electrical conductivity measurements rapidly characterize nanoparticle size and concentration in suspension (Figure 3). A particularly exciting aspect of this approach is the ability to construct microfluidic-based characterization tools using thermal transfer films, completely eliminating the need for cleanroom facilities. We demonstrate the application of these simple devices to enable in-situ monitoring of continuous nanoparticle synthesis (Figure 3a). The measured electrical resistance response can reveal information about particle concentration or size during chemical reaction, and consequently is able to

deliver instantaneous feedback to appropriately manage synthesis conditions. We also demonstrate the ability of this approach to function offline using only microliter samples and a low-cost multimeter (Figure 3b).

CHAPTER II

EXPERIMENTAL METHODS AND COMPUTATIONAL MODEL*

Experiment Methods

Nanomaterials and Suspension Preparation

Aqueous suspensions were prepared by dispersing commercial nanoparticle powders in deionized water, followed by 20 s of agitation using a digital vortex mixer (Cat. No. 02215370; Fisher Scientific). All nanoparticle powders were used as received from the manufacturer in order to assess the capability of analyzing commercial samples. Materials employed in these studies are summarized in Table 1

PDMS Molding and Device Assembly

Y-shaped microchannels (40 μm tall, 500 μm wide, 2.4 cm long) were constructed in poly(dimethyl siloxane) (PDMS) using standard soft lithography. Master molds were prepared by spin coating SU-8 2025 photoresist onto silicon wafers, followed by a standard soft bake, UV exposure through the transparency film via a mask aligner, and development of the imprinted pattern. A freshly prepared PDMS mixture (10:1 volume ratio of base to crosslinker; Sylgard 184; Dow Corning) was degassed under vacuum and poured over the master mold to cast the microchannel structures. After curing at 80 ℃ for 2 h, the mold was cooled to room temperature and individual microchannels were peeled away. Inlet and outlet holes were punched using a syringe

---

* Reprinted with permission from "Localized Fluorescent Complexation Enables Rapid Monitoring of Airborne Nanoparticles", F. Meng, M. D. King, Y. A. Hassan and V. Ugaz, 2014, *Environmental Science: Nano*, 358-366, Copyright 2014 by Royal Society of Chemistry.

needle, and the PDMS structures were bonded to glass microscope slides after O_2 plasma treatment in a reactive ion etcher. Polyethylene tubing was inserted into the inlet and outlet holes to make fluidic connections.

Electrodes Fabrication and Assembly with Microchannel

Substrates were prepared by metal sputter (Lesker PVD 75, sputter ignition 250W, gas 3mTorr Argon) depositing a 100 nm-thick copper layer on glass slides (Fisherbrand, Cat. No. 12-550-A3, precleaned by vendor and sonicating in Acetone for 10 min before use). Electrode designs were drawn using (Microsoft Word) and printed on thermal transfer film (Press-n-peel, Cat. No. PNPB20, Techniks Inc) using a laser printer (HP Q5959A) (Cho, Parameswaran, & Yu, 2007). The printed film was aligned to the substrate, heated using iron (how was heat applied, under pressure?) for 5 min, and peeled away leaving the toner pattern on the copper surface. The temperature setting on the iron is critical due to the specification of laser printer and a suggested starting is 135-165 ^{o}C under generally setting between "acrylic" and "polyester" for iron. The substrate was then etched for 30 s (Gold Etch-TFA Type, Transene Company Inc) and rinsed, after which the toner was stripped using acetone (Fisher Scientific, Certified ACS, Lot No. A18-4). Despite its simplicity, the thermal transfer process yields sufficient resolution for this application (1 – 2 mm-wide electrodes spaced apart, layout inserted in Figure 4a). The copper metal also provides a surface amenable to soldering leads for external electrical connections. Electrode array designs are provided in the supporting information. Microchannels were fabricated in poly(dimethyl siloxane) (PDMS) (10:1 volume ratio of base to crosslinker, Sylgard 184, Dow Corning) using master molds

constructed from SU-8 2025 photoresist (MicroChem Corp) via standard methods (Meng et al., 2014), and bonded to the glass slides by O_2 plasma treatment in a reactive ion etcher (March Plasma Systems Model CS-1701). Even with the copper metallization, sufficient bond strengths were achieved to support flow rates up to 4 mL/min within 2.4 cm-long microchannels of 500 x 40 μm cross-section without leaking (Figure. 4b). Before each experiment, polyethylene tubing was inserted into the inlet and outlet holes to make fluidic connections.

Spectrofluorometer Experiments

Steady-state emission spectra of nanoparticle suspensions, dye solutions, and multi-component mixtures were measured using a PTI QuantaMaster series spectrofluorometer. A xenon arc lamp (490 nm peak wavelength) was warmed up to 75 watts and steady state excitation was applied to the sample via a 495 nm long-pass filter. A digital emission scan from 500 to 800 nm was used with 1 nm step size and 0.1 second integration. 1~2 mL samples were loaded in cuvettes for analysis. Peak values of the intensity versus emission wavelength profiles were acquired and are expressed as relative intensity in bulk spectrofluorometer data.

Microchannel Operation and Image Acquisition

Continuous analysis was performed by co-injecting nanoparticle suspensions and the fluorescein tracer into the inlets of a y-shaped microchannel using a syringe pump (Model KDS7230, KD Scientific Inc.) at flow rates ranging from 0.002 to 0.2 mL/min (0.02 mL/min was used unless otherwise indicated). Images were analyzed to obtain descriptors of interfacial fluorescence phenomena summarized in Figure 1 of the main

text. Imaging was performed along the mid-plane of the microchannel to minimize sidewall effects. A flow rate of 0.02 mL/min (corresponding average velocity of 0.033 m/s) and 1.2 cm downstream image acquisition position yields characteristic residence times in the microchannel in the vicinity of 0.36 s.

The TiO_2 nanoparticles are synthesized by wel-known hydrolysis of titanium tetraisoproxide (TTIP)(Cottam, Krishnadasan, deMello, deMello, & Shaffer, 2007). To maintain proper reaction rate and produced nanoparticle size various volumes of TTIP was diluted by IPA to 10 mL for synthesis reagent in microchannel device and batch. KCl as electrolytes was added into DI water to get a 0.2 mol/mL prepared solution to provide considerable electrical conductivity. 3 mL prepared KCl solution was later dispersed by IPA to 10 mL for synthesis reagent. We used a Y-shape channel to mix dispersed TTIP and dispersed KCl water solution, allowing TiO_2 to be synthesized in the channel. The channel was enclosed with PDMS channel replica and PDMS slide instead of glass, to avoid significant sedimentation occurring when glass slide was used. The hydrolysis is very fast and white flocculent particles were observed inside microchannel. A 1 meter tube was used to induce synthesized TiO_2 nanoparticle suspension into microchannel inserted with copper electrodes, and to ensure fully mixing and reacting of two inlet streams. The 100 μL/min flow rate was used to infuse dispersed TTIP and dispersed KCl water solution through Y-shape channel mixer and connection tube to the electrode-inserted channel for electrical resistance measurement. After solutions are infused into the measuring channel, the flow rate is reduced to 1 μL/min for more stable measurement by reducing influence of flowing fluctuation. Same resistance

measurement by LCR inside microchannel was used as the same for the samples from commercial TiO_2 powders and samples from synthesized TiO_2 were collected for SEM examination.

Scanning Electron Microscopy

Scanning electron microscopy (SEM) images of the nanoparticles were obtained using a JEOL JSM-6400 at an accelerating voltage of 5 keV and 7.5 mm working distance with SEI detector. Samples were prepared from dried suspensions. Images were taken with a 100 nm scale bar. To determine the nanoparticle size, each distinguishable nanoparticle was circumscribed and its size was calculated by circle area. Ensembles of at least 100 particles were analyzed to give size distributions. Size distribution data for the ZnO and TiO_2 materials used in the main text are provided in Figure 5. Alternatively, synthesized TiO_2 nanoparticles (which appear ~10 nm) were coated above with 3 nm platinum by sputter coater (Cressington, Ted Pella, inc) to get better images. JEOL JSM-7500F SEM was used under accelerate voltage 3.0 kv, emission current 9 μA, probe current 10, work distance around 5.5 mm.

Dynamic Light Scattering

Dynamic light scattering (DLS) measurements were performed using a ZetaPALS instrument with a BI-9000AT correlator (Brookhaven Instruments Corp.). Anatase nanoparticles were dispersed in DI water at concentrations ranging from 0.002 to 0.03 wt%. Time-averaged particle size distributions were collected over an analysis period of at least 5 min at room temperature. Three separate measurements were acquired for each freshly prepared solution. The wavelength of the incident laser beam

(λ) was 660 nm, and the detector angle (λ) was 90 °. Autocorrelation functions were deconvoluted using the built-in nonnegatively constrained least squares-multiple pass (NNLS) algorithm in order to obtain particle size distribution. Particle sizes measured with DLS were considerably higher than those determined via SEM analysis, likely due to the presence of agglomerates in the samples. Figure 6 shows representative data for anatase TiO_2 nanoparticles with 49 ± 9 nm mean diameter (Cat. no. 637254, Sigma-Aldrich), where the DLS analysis reports a mean size of 330 nm. Similar results were obtained with all nanomaterials tested.

Airborne Nanoparticle Collection and Analysis

The nano aerosol collection system consisted of a 200 L min^{-1} low cutpoint WWC (cutpoint <400 nm AD, concentration factor $>10^6$). Collection efficiency in this size range was enhanced by modifying the design of the liquid injection system, liquid skimmer, and aerosol inlet. A cutpoint reduction was accomplished by optimizing the slot dimension. Dilutions of aqueous Al_2O_3 nanoparticle suspensions were prepared in MQ H2O and delivered through a 200 mm diameter, 180 cm long tube using a Collison 6-jet atomizer (BGI, Inc.).

The aerosolized nanoparticles were then sampled using the WWC in a collection liquid containing 0.1 mg mL^{-1} Tween 20. Each sample was aerosolized and collected for a 15 min period, with an additional 5 min washing cycle performed while the atomizer was turned off. Filter-based reference collections were also performed using 47 mm A/E filters (Pall Corp.) during the 15 min aerosolization and collection periods (nanoparticles

were weighed before being introduced into the chamber and after collection on the filter and with the WWC (from the dried collection fluid) to evaluate collection efficiency).

The size and concentration of the aerosolized nanoparticles in the flow chamber was quantified using a Scanning Mobility Particle Sizer (SMPS; Model 3936; TSI, Inc.) equipped with an electrostatic classifier (Model 3080) and a nano differential mobility analyzer (Model 3085). We found that this configuration provided an optimal resolution of particle sizes in the ultrafine sub-150 nm range. Nanoaerosol components with particle sizes >523 nm were analyzed with an Aerodynamic Particle Sizer spectrometer (APS; Model 3321; TSI, Inc.) to verify that no particle agglomeration occurred during aerosolization. The WWC collections were quantified in the 10–2000 nm range using a NanoSight LM 10 microscope (NanoSight Ltd.) with the Nanoparticle Tracking Analysis (NTA) Version 2.0 software.

Electrical Measurement

The continuous synthesis and quality control of on-purpose nanoparticle is schemed in Figure 3. The resistance of flow segment is detected by LCR meter (Keithley).The Keithley Model 2100 applies a constant DC current to the unknown resistance and then measures the voltage. The resistance is calculated from ratio of these values according to the test currents: the test current is 1mA for 100 and 1 kohm resistance range; 100uA for 10k ohm range; 10uA for 100k ohm range; 5uA for 1M ohm range; 500nA for 10M and 100M ohm ranges.

The EC of suspensions by batch were measured by using of an ExStik 400EC meter (Extech Instruments Corp). The EC of suspensions in microchannel by offline

mode were measured by using of a commercial 85 XT Digital Mutimeter (Wavetek Meterman).

Physico-chemical and Flow Model

Physico-chemical Model

A primary consideration in the development of our model involves quantifying how the available surface adsorption sites (a key parameter governing fluorescent complexation) are related to the bulk oxide concentration in suspension (the most convenient observable quantity). We accomplish this by expressing surface binding site concentration $[N_s]$ is terms of the nanomaterial's molar concentration $[M]_i$ via $[N_s] = N [M]_i$ (N expresses the binding sites per mole of nanomaterial; i.e., binding sites per nanoparticle / moles of nanomaterial per nanoparticle). It can be inferred that the parameter N increases as nanoparticle size decreases due to the higher surface area to volume ratio.

At equilibrium, fluorescent complexation can be represented by a stoichiometric balance of the form $[N_s] + p[D] \overset{K}{\rightleftharpoons} [ND]$,

where p represents the number of dye molecules associated with each surface binding site and [ND] is the molar concentration of sites occupied by dye nanoparticle complexes. The equilibrium constant K is expressed in terms of association and disassociation steps as

$$K = \frac{k_{on}}{k_{off}} = \frac{\left[\mathrm{ND}\right]_{eq}}{\left[\mathrm{N_s}\right]_{eq}\left[\mathrm{D}\right]_{eq}^{p}} \tag{1}$$

where the surface sites available for complexation are represented by $[N_s]_{eq} = N\,[M]_i - [ND]_{eq}$ and the free dye available for complexation is obtained from $[D]_{eq} = [D]_i - p[ND]_{eq}$, making these substitutions yields.

$$K = \frac{[ND]_{eq}}{[N_s]_{eq}[D]_{eq}^{p}} = \frac{[ND]_{eq}}{\left(N[M]_i - [ND]_{eq}\right)\left([D]_i - p[ND]_{eq}\right)^{p}} \tag{2}$$

Equation (2) can be rearranged to obtain an expression for $[ND]_{eq}$ as a function of $[M]_i$ and $[D]_i$, as well as constants N and K. In this way, the nanoparticle concentration in suspension $[M]_i$ can be correlated with the observed fluorescence signature via its dependence on $[ND]_{eq}$ if the initial dye concentration $[D]_i$ is known.

$$[M]_i = \frac{[ND]_{eq}}{N}\left(\frac{1}{K\left([D]_i - p[ND]_{eq}\right)^{p}} + 1\right) \tag{3}$$

The parameters N, K, and p are obtained by performing bulk spectrofluorometer measurements under equilibrium conditions to quantify the dependence of the observed fluorescence intensity F_{obs} across an ensemble of dye and nanoparticle concentrations. To accomplish this, the fluorescence is decomposed into contributions from the free dye (F_D) and bound nanoparticle-dye complexes (F_{ND}) via $F_{obs} = F'_D + F'_{ND}$. The absolute fluorescence variables are more conveniently expressed in terms of scaled quantities $F'_D = F_D\,([D]_{eq} / [D]_i)$ and $F'_{ND} = F_{ND}\,(p\,[ND]_{eq} / [D]_i)$ reflecting the observation that $[ND]_{eq} = 0$ and $F_{obs} = F_D$ when the sample contains only tracer, whereas $[ND]_{eq} = [D]_i$ and $F_{obs} = F_{ND}$ when all the dye is complexed with nanoparticles. Applying the stoichiometric relationship between $[D]_{eq}$ and $[ND]_{eq}$ yields.

$$F_{obs} = F_D \frac{[\mathrm{D}]_{eq}}{[\mathrm{D}]_i} + F_{ND} \frac{[\mathrm{ND}]_{eq}}{[\mathrm{D}]_i / p} = F_D \frac{[\mathrm{D}]_i - p[\mathrm{ND}]_{eq}}{[\mathrm{D}]_i} + F_{ND} \frac{p[\mathrm{ND}]_{eq}}{[\mathrm{D}]_i} \quad (4)$$

Upon rearranging and solving for $[\mathrm{ND}]_{eq}$, we obtain.

$$[\mathrm{ND}]_{eq} = \frac{F_{obs} - F_D}{F_{ND} - F_D} \frac{[\mathrm{D}]_i}{p} \quad (5)$$

It is convenient to combine the free and complexed dye contributions by expressing them in terms of the ratio $R = F_{ND} / F_D$. Finally, substituting equation (5) into (3) and incorporating the definition of R enables the observed fluorescence Fobs to be related to the concentration of suspended nanoparticles $[\mathrm{M}]_\mathrm{i}$.

$$[\mathrm{M}]_\mathrm{i} = \frac{1}{N}\left(\frac{F_{obs} - F_D}{(R-1)F_D}\frac{[\mathrm{D}]_\mathrm{i}}{p}\right)\left(\frac{1}{K\left(\frac{RF_D - F_{obs}}{(R-1)F_D}[\mathrm{D}]_\mathrm{i}\right)} + 1\right) \quad (6)$$

The constants N, K, R and p in equation (6) are obtained from fitting to data from a series of bulk spectrofluorometric measurements as a function of tracer dye and nanoparticle concentration. The results of applying this analysis to 60 ± 20 nm ZnO nanoparticles are shown in Figure 7a of the main text. The Matlab function nlinfit was applied to simultaneously determine the parameter set of N, K, and R using an iterative least squares process, yielding the best simultaneous fit to data obtained at three different tracer dye concentrations for values of p ranging from 1 to 8 (Figure 8). For example, at p = 5 with initial guesses of K = 4,000, N = 0.015, and R = 4, output values of K = 4,240, N = 0.0161, R = 3.88 were obtained. Selection of an appropriate p value was guided by a desire to attain a realistic value of the fitted coefficient N in the vicinity of 0.02 or less (e.g., when N = 0.02, the surface density of effective binding sites = 8.3 sites/nm^3,

exceeding realistic density limits for metal oxide nanoparticles (Mueller, Kammler, Wegner, & Pratsinis, 2003)).

Consequently, we applied $p = 5$ for all subsequent analysis of ZnO, corresponding to a value of $N = 0.016$. Although similar phenomena have been considered in previous studies, two important assumptions are generally applied in order to simplify the analysis (Kathiravan, Chandramohan, Renganathan, & Sekar, 2009). First, comparable fits are often performed using the bulk oxide concentration, leading to values of N that are not consistent with the physically possible density of effective adsorption sites. Second, saturation conditions are assumed whereby the quantity of available binding sites is much greater than the number of available dye molecules. Our analysis is not subject to these simplifications, leading to binding constants that differ somewhat from other reported values.

We next extended the results obtained for 60 nm particles to enable analysis of spectrofluorometric measurements obtained from 117 ± 37 and 144 ± 41 nm ZnO nanoparticles (Figure 7b). The value of R is assumed to remain constant because the nature of the chemical interactions associated with particle-tracer complexation is fundamentally unchanged for the same combination of nanomaterial and dye. The coefficient N is determined by scaling the value obtained at 60 nm to other particle sizes via its dependence on the surface to volume ratio.

Equation (6) can then be applied to fit the concentration dependent fluorescence data at $p = 5$ to determine the equilibrium constant K, which in turn guides selection of

the kinetic parameters k_{on} and k_{off} corresponding to each particle size. Parameters obtained in our analysis of ZnO nanoparticles (Figure 7) are given in Table 2.

We remark that polydispersity effects are inherently embedded into our model by virtue of the fact that its parameters (*N*, *K*, *p)* are obtained from bulk spectrofluorometer measurements in (Figure. 7a). Although strictly speaking these parameters may be size dependent, this is a reasonable compromise in the absence of monodisperse calibration samples, and in consideration of our envisioned characterization applications where sharply bi-modal or multi-modal size distributions are not anticipated (i.e., our method is highly amenable to enable rapid online analysis in manufacturing settings where properties are not expected to significantly deviate beyond a well-defined window). To validate this hypothesis, we simulated the fluorescence response from an ensemble of particles binned to mimic the size distributions of 60 and 144 nm nanoparticle samples employed to obtain kinetic model parameters (size distributions and SEM data shown in Figure. 7b). The full ensemble of coupled multiple dye-nanoparticle reactions involving each particle size in the distribution was evaluated and combined to generate the collective fluorescence signature (see Table 2 for parameters applied in the computational model). The results of this analysis (open square symbols in Figure 7c) display close agreement with our initial model predictions where polydispersity was not explicitly included (solid line in Figure 7c). Since our model is effectively "trained" using samples displaying size distributions similar to those expected to be encountered in its practical application, it is therefore reasonable to expect that large deviations from

the resulting predictions are unlikely under conditions the particle size distribution profiles display similar characteristics.

The same general procedure was followed for analysis of anatase and rutile TiO_2 mixtures; however parameter selection was constrained by our desire to maintain the same particle size between species. Additionally, the concentration dependent trends observed in the spectrofluorometer data (initial decrease at low concentration in anatase, and quenching in rutile) incorporate additional complexities not fully captured by the framework in equation (6).

We therefore selected a representative parameter set based on insights from our previous analysis for the purpose of evaluating the ability to characterize multi-component mixtures. Parameters obtained in our analysis of TiO_2 nanoparticles (Figure 9) are given in Table 3.

Flow Model

The kinetic parameters k_{on} and k_{off} are used as inputs for a flow model to predict the interfacial fluorescence intensity profiles observed in our microchannel-based experiments (i.e., Figure 1). Following the framework developed by Yager et. al. for analysis of microfluidic immunoassays (Foley, Nelson, Mashadi-Hossein, Finlayson, & Yager, 2007; Hatch, Garcia, & Yager, 2004; Hatch et al., 2001; Kamholz, Weigl, Finlayson, & Yager, 1999; Nelson, Foley, & Yager, 2007), we constructed a 2D flow model using COMSOL Multiphysics to solve the steady-state Navier-Stokes equations (representing the flow field) simultaneously with a system of partial differential

equations expressing coupled convection-diffusion processes with surface reactions (representing nanoparticle-tracer complexation).

$$\rho\frac{\partial \boldsymbol{u}}{\partial t}+\rho\boldsymbol{u}\bullet\nabla\boldsymbol{u}=-\nabla p+\mu\nabla^2\boldsymbol{u} \tag{7a}$$

$$\frac{d\left[\mathrm{D}\right]}{dt}+\nabla\bullet\left(-\alpha f\nabla\left[\mathrm{D}\right]+\left[\mathrm{D}\right]\boldsymbol{u}\right)=p\left(k_{off}\left[\mathrm{ND}\right]-k_{on}\left[\mathrm{N_S}\right]\left[\mathrm{D}\right]^p\right) \tag{7b}$$

$$\frac{d\left[\mathrm{N_S}\right]}{dt}+\nabla\bullet\left(-\alpha\nabla\left[\mathrm{N_S}\right]+\left[\mathrm{N_S}\right]\boldsymbol{u}\right)=k_{off}\left[\mathrm{ND}\right]-k_{on}\left[\mathrm{N_S}\right]\left[\mathrm{D}\right]^p \tag{7c}$$

$$\frac{d\left[\mathrm{ND}\right]}{dt}+\nabla\bullet\left(-\alpha\nabla\left[\mathrm{ND}\right]+\left[\mathrm{ND}\right]\boldsymbol{u}\right)=-k_{off}\left[\mathrm{ND}\right]+k_{on}\left[\mathrm{N_S}\right]\left[\mathrm{D}\right]^p \tag{7d}$$

Fluid properties were assumed to be those of water at room temperature, and size-dependent nanoparticle diffusivity coefficients were estimated using the Stokes-Einstein relationship as $\alpha = k_B T / (3\pi\mu d)$. Boundary conditions and variables are listed in Tables 4 and 5

Poly Disperse Physico-chemical Model

A more detailed model formulation can be obtained by considering the poly disperse nature of the commercial nanoparticles involved our experiments. This can be accomplished by dividing the population of nanoparticles into discrete groups or bins based on their size range. Individual surface reaction and association/disassociation equilibrium equations can then be written for each size bin group as follows.

$$\left[\mathrm{N_{s_i}}\right]+p\cdot\left[\mathrm{D}\right]\overset{K_i}{\leftrightarrow}\left[\mathrm{ND}_i\right] \tag{8}$$

$$K_i=\frac{k_{on}}{k_{off}}=\frac{\left[\mathrm{ND}_i\right]_{eq}}{\left[\mathrm{N_{s_i}}\right]_{eq}\left[\mathrm{D}\right]_{eq}^{p}}=\frac{\left[\mathrm{ND}_i\right]_{eq}}{\left(\left[\mathrm{N_{s_i}}\right]-\left[\mathrm{ND}_i\right]_{eq}\right)\cdot\left(\left[\mathrm{D}\right]-p\cdot\sum\left[\mathrm{ND}_i\right]_{eq}\right)^{p}} \tag{9}$$

The subscript *i* indicates group number and *eq* indicates chemical concentration under equilibrium state. The equations can be further rearranged according to stoichiometry to obtain the form

$$K_i = \frac{k_{on}}{k_{off}} = \frac{[\mathrm{ND}_i]_{eq}}{[\mathrm{N_{s_i}}]_{eq}[\mathrm{D}]_{eq}{}^{p}} = \frac{[\mathrm{ND}_i]_{eq}}{\left([\mathrm{N_{s_i}}] - [\mathrm{ND}_i]_{eq}\right) \cdot \left([\mathrm{D}] - p \cdot \sum [\mathrm{ND}_i]_{eq}\right)^{p}} \tag{10}$$

$$K_i \cdot \left([\mathrm{N_{s_i}}] - [\mathrm{ND}_i]_{eq}\right) \left([\mathrm{D}] - p \cdot \sum [\mathrm{ND}_i]_{eq}\right)^{p} - [\mathrm{ND}_i]_{eq} = 0 \tag{11}$$

$$\frac{K_{ave} \cdot d_{ave}}{d_i} \cdot \left(\frac{N_{ave} \cdot d_{ave}}{d_i} \cdot mol\%_i \cdot [\mathrm{M}] - [\mathrm{ND}_i]_{eq}\right) \cdot \left([\mathrm{D}] - p \cdot \sum [\mathrm{ND}_i]_{eq}\right)^{p} - [\mathrm{ND}_i]_{eq} = 0 \tag{12}$$

In the above equation, *mol%* is the molecular percentage of each particle group in the ensemble. $K_i = \frac{K_{ave} \cdot d_{ave}}{d_i}$ and $N_i = \frac{N_{ave} \cdot d_{ave}}{d_i}$ are correlated to the particle size within each bin d_i, the average particle size d_{ave}, and the corresponding values of *K* and *N* when $d = d_{ave}$ (K_{ave} and N_{ave} are constants). The average size for a total *n* groups of particles can be calculated based on the arithmetic mean $d_{ave} = \frac{1}{n}\sum_{i=1}^{n} d_i$ and cubic mean $d_{ave} = \left(\frac{1}{n}\sum_{i=1}^{n} {d_i}^3\right)^{1/3}$

The arithmetic mean is a number mean (more accurately a number length mean), which is obtained by summing all the diameters and dividing the sum by the number of particles. It is the most direct reflection to compare the particles on the basis of length. The cubic mean is a number-volume or number-weight mean, which is calculated by cubing and summing the diameters, dividing the sum by the number of particles and taking a cube root to get back to a mean diameter. It is used to compare the particles on

the basis of weight. It is beneficial to compare the models with the particle number means on basis of different physical implications.

Equation (12) can be further rearranged based on the relationship between *mol%* (molecular percentage) and *number%* (particle number percentage) for each group

$$mol\%_i = \frac{number\%_i \cdot d_i^3}{\sum(number\%_i \cdot d_i^3)}$$

$$\frac{K_{ave} \cdot d_{ave}}{d_i} \cdot \left(\frac{N_{ave} \cdot d_{ave}}{d_i} \cdot \frac{number\%_i \cdot d_i^3}{\sum(number\%_i \cdot d_i^3)} \cdot [\mathrm{M}] - [\mathrm{ND}_i]_{eq} \right) \cdot \left([\mathrm{D}] - p \cdot \sum [\mathrm{ND}_i]_{eq} \right)^p - [\mathrm{ND}_i]_{eq} = 0 \quad (13)$$

We also have the scaling to decompose the observed fluorescence into contributions from the free dye and bound nanoparticle-dye complexes in each group.

$$F_{observe} = F_D \cdot \frac{[\mathrm{D}]_{eq}}{[\mathrm{D}]} + F_{ND} \cdot \frac{\sum [\mathrm{ND}_i]_{eq}}{[\mathrm{D}]/p} = F_D \cdot \frac{[\mathrm{D}] - R \cdot p \cdot \sum [\mathrm{ND}_i]_{eq}}{[\mathrm{D}]} \quad (14)$$

So far, we have obtained similar equations for nonlinear regression as in the previous section where polydispersity was not considered. The major difference is that here we need to first solve for a set of equilibrium concentrations of bound nanoparticle-dye complexes $[\mathrm{ND}_1]_{eq}, [\mathrm{ND}_2]_{eq}, \ldots, [\mathrm{ND}_i]_{eq}$ in each group of particles comprising the size distribution profile.

An example is constructed based on the bulk spectrofluorometric data of 60 $\pm$20 nm ZnO particles in Figure 7a. The particles are grouped according to bins with 20 nm range as shown in Table 6. The values of molecular percentage (mol%) are calculated based on the values of particle number percentage (number%), which comes from the histogram of ZnO particle size distribution in Figure 5. The constants *N*, *K*, *R* and *p* are

obtained from nonlinear regression of bulk spectrofluorometric measurements as a function of tracer dye and nanoparticle concentration shown in Table 7.

Table 7 compares values of the parameters *N, K, R* obtained in the mono disperse model with those obtained from the polydisperse model when the average particle size is calculated via arithmetic and cubic methods. It is seen parameters determined with the cubic average particle size are closer to those obtained from the mono disperse model. Among all these models, the sums of the squared residuals are virtually identical, indicating the quality of these nonlinear regressions are equivalent. This analysis proves that the mono disperse model can be a useful short-cut candidate to obtain kinetic parameters without significantly compromising accuracy.

CHAPTER III

INSTANTANEOUS PHYSICO-CHEMICAL ANALYSIS OF SUSPENSION-BASED NANOMATERIALS

Fluorescent Complexation Reveals Concentration, Size, and Species Information

To illustrate how this interfacial signature depends on properties of suspended nanomaterials, we characterized interactions between ZnO (60 ± 20 nm) and TiO_2 (anatase: 49 ± 9 nm and 137 ± 36 nm, rutile: 40 ± 7 nm) nanoparticles with a fluorescein tracer. Fluorescence enhancement is observed in ZnO and anatase TiO_2, whereas quenching is observed in rutile TiO_2 (Figure 10a). In the case of ZnO, a strong concentration dependence can be resolved over 4 orders of magnitude in nanoparticle concentration (Figure 10b). This wide sensitivity range is made possible by combining interfacial (optimal at higher concentrations) and lateral (optimal at low concentrations) fluorescence intensity data (Figure 1b), yielding results consistent with conventional bulk spectrofluorometer measurements. The underlying complexation phenomena reflect interactions between Zn^{2+} ions in the ZnO matrix and carbonyl groups in the tracer (Zhang et al., 2010). The fluorescence signatures are also dependent on particle size, as seen by comparison of data from suspensions containing 49 and 137 nm anatase TiO_2, where a 4-fold intensity increase is observed in the smaller diameter material (Figure 10c). Enhanced sensitivity to smaller particle sizes is a unique feature of our approach, and reflects the inherently surface-dominated Complexation mechanism that is most pronounced at the smallest particle sizes where the surface area to volume ratio is

maximized (Auffan et al., 2009). Remarkably, this size dependent sensitivity is achievable regardless of the material's agglomeration state, as can be seen upon comparison with DLS data suggesting that the characteristic diameters of both materials are > 200 nm. This discrepancy emerges because scattering techniques are unable to clearly discern clustering of small-sized nanoparticles into agglomerates with dimensions comparable to individual larger nanoparticles (SEM insets in Figure 10c). Our approach also reveals isoforms in crystalline morphology, as demonstrated in the case of TiO_2 where fluorescence enhancement observed in anatase samples transforms to quenching in the rutile isoform (Figure 10d).

ZnO Nanoparticle Analysis and Model Verification

We developed a physical model that captures the interplay among particle species, size, and concentration governing these fluorescence signatures (Figure 7). Our model is based on considering the number of available surface binding sites on the suspended nanoparticles [N_s], which is in turn related to the nanomaterial's molar concentration $[M]_i$ via $[N_s] = N\,[M]_i$ (N expresses the binding sites per mole of nanomaterial; i.e., binding sites per nanoparticle / moles of nanomaterial per nanoparticle). At equilibrium, these complexation interactions can be represented by a stoichiometric balance of the form $[N_s] + p[D] \overset{K}{\rightleftharpoons} [ND]$, where p represents the number of fluorescein molecules associated with each surface binding site and [ND] is the molar concentration of sites occupied by dye-nanoparticle complexes. The equilibrium constant K is expressed in terms of association and disassociation steps as

$K = \frac{k_{on}}{k_{off}} = \frac{\left[\mathrm{ND}\right]_{eq}}{\left[\mathrm{N_s}\right]_{eq}\left[\mathrm{D}\right]_{eq}^{p}}$ where the surface sites available for complexation are represented by $[N_s]_{eq} = N\,[M]_i - [ND]_{eq}$ and the free dye available for complexation is determined from $[D]_{eq} = [D]_i - p[ND]_{eq}$. Combining these expressions enables the nanoparticle concentration in suspension $[M]_i$ to be correlated with the observed fluorescence signature via its dependence on $[ND]_{eq}$. The constants *N*, *K*, *p*, and *R* (a parameter expressing the relative fluorescence intensity of the free and bound tracer) are determined by fits to data obtained from a series of bulk spectrofluorometric measurements as a function of tracer and nanoparticle concentration (Figure 7a). The equilibrium constant *K* is then used to guide selection of k_{on} and k_{off} values employed in a reaction-diffusion flow model that quantitatively predicts the fluorescence signatures observed in our microchannel-based experiments.

We applied this framework toward analysis of ZnO nanoparticles, enabling the interdependence among particle size, species, and concentration to be expressed in terms of a surface plot construction uniquely relating experimentally measured fluorescence to the compositional state of the suspended nanomaterials (Figure 7b). This fingerprint makes it possible to instantaneously extract size and/or concentration information from unknown samples via a single microchannel-based fluorescence measurement. To illustrate how this capability could be implemented in a setting relevant to manufacturing, we measured interfacial fluorescence intensities of aqueous suspensions prepared from four different commercial ZnO nanopowders (Figure 7c). Particle sizes ranged from 64 to 191 nm, and suspension concentrations were held constant at 0.02

wt%. Fluorescence data obtained in the microchannel format yield mean particle sizes that agree remarkably well with the model prediction in Figure 7b, especially considering the inherently heterogeneous particle size distributions and the assumptions involved in our model formulation. Our approach therefore makes it straightforward to continuously monitor nanoparticle size directly in suspension, enabling routine online characterization.

Analysis of Anatase and Rutile TiO_2 Nanoparticle Mixtures

A manufacturing scenario of particular importance involves ensuring that consistent relative amounts of anatase and rutile species are maintained in multi-component mixtures of TiO_2 nanoparticles. Our method can be readily adapted to perform this characterization in a continuous format by exploiting the distinct fluorescence signatures displayed by each component (Figure 10). Although nanoparticle-tracer complexation occurs via a similar pathway in each species, differences in the band gap between energy levels lead to fluorescence enhancement in the anatase form and quenching in the rutile species (Ranade et al., 2002; Scanlon et al., 2013). The relative quantity of each isoform present in the mixture can thus be determined by simultaneous analysis of interfacial intensity and lateral shift information, where the same framework we developed for ZnO nanoparticles is applied to evaluate kinetic parameters (Figure 9a). Our model successfully captures the observed trends of increased intensity and reduced lateral shift with increasing fraction of anatase TiO_2 in the overall solid content, enabling the fluorescence intensity and lateral shift to be predicted across a range of compositional states (Figure 9b, compositions are expressed

in terms of the anatase mass fraction, anatase / (anatase + rutile) = A / (A + R)). Cross-plotting these data then enables the anatase fraction to be uniquely determined from these simultaneously measured observables (Figure 9c). Precise control over the compositional profile of mixed-phase TiO_2 nanoparticles is a critical factor governing photocatalytic reaction performance (Ohno et al., 2001), solar conversion efficiency (G. H. Li et al., 2009), and toxicity (Gerloff et al., 2012), Notably, many of these applications involve mixtures containing optimal anatase fractions ranging from 0.75 ~ 0.99 (Kim & Ehrman, 2009; G. H. Li et al., 2009), well within the analytical range of our method. The lateral shift does not display a strong composition dependence under these conditions, leaving interfacial intensity as the primary quantity of interest. Our model displays good agreement with experimentally measured values of interfacial intensity spanning a range of compositional states (Figure 9c), enabling detailed in-situ characterization information to be continuously extracted from microchannel based fluorescence measurements.

Conclusion

Compared with conventional characterization based on x-ray diffraction (Ohno et al., 2001; Testino et al., 2007), a batch technique requiring dry powder samples, the speed and simplicity of our continuous in-situ approach combined with its ability to provide both size and compositional information offers compelling advantages for routine compositional monitoring in nanomanufacturing settings (e.g., to ensure that material properties are maintained within clearly defined limits). Our methodology is inherently versatile and can be readily applied to establish fluorescence signature

fingerprints of complex (and more realistic) suspension-based nanomaterial products incorporating coatings and stabilizing additives. Few currently available techniques are able to instantaneously deliver this kind of quantitative characterization in an online format, suggesting broad applicability as a routine tool that can supplement the workhorse analytical methods in a host of emerging manufacturing settings.

CHAPTER IV

LOCALIZED FLUORESCENT COMPLEXATION ENABLES RAPID MONITORING OF AIRBORNE NANOPARTICLES[*]

Species and Size Dependence of Fluorescent Complexation

Considering the match points between our device and critical need for environmental monitoring, we demonstrated one of practical utility by integrating our device into a environmental monitor. We first examined the concentration dependence of interfacial fluorescence by co-injecting fluorescein dye into the microchannel in parallel with suspensions of Al_2O_3 (23 $\pm$3 nm), TiO_2 (49 $\pm$9 nm), Fe_2O_3 (28 $\pm$5 nm), CuO (31 $\pm$ 9 nm), SiO_2 (21 $\pm$4 nm), and ZnO (60 $\pm$20 nm) nanoparticles (Figure 11a, see Figure 12 for characterization data). This panel of oxide-based species was selected to represent some of the most commonly encountered nanomaterials, and the molar concentration of each was held constant based on the formula weight of its constituent molecules (we chose this basis rather than the number of particles to avoid introducing uncertainties associated with the particle size distribution and morphology). Fluorescence from Al_2O_3 displays a characteristic pattern of focused interfacial intensity accompanied by an adjacent depletion zone in the dye stream, consistent with previous observations (Ozturk, Hassan, & Ugaz, 2010). Since the depletion zone enables interfacial fluorescence to be clearly isolated, we selected this formulation for subsequent airborne sampling studies.

---

[*] Reprinted with permission from "Localized Fluorescent Complexation Enables Rapid Monitoring of Airborne Nanoparticles", F. Meng, M. D. King, Y. A. Hassan and V. Ugaz, 2014, *Environmental Science: Nano*, 358-366, Copyright 2014 by Royal Society of Chemistry.

Even greater fluorescence enhancements were observed with TiO_2 and ZnO nanoparticles, overwhelming the adjacent depletion zone. Similar effects have been previously reported in ZnO nanoparticles and are generally explained in terms of interactions between Zn^{2+} ions in the ZnO matrix and carbonyl groups in the dye (Zhang et al., 2010). Interfacial fluorescence is also sensitively dependent on particle size, as seen by comparison of data from suspensions containing 60, 117, and 144 nm ZnO (Figure 11b, c). Fluorescence intensity is maximized at small particle sizes – a distinguishing feature of our approach that reflects the inherently surface-dominated nanoscale Complexation mechanism (Grassian, 2008). Unlike conventional mass-based analytical methods, sensitivity is most pronounced at the smallest particle sizes where the surface area to volume ratio is maximized. The observed fluorescence is proportional to the particle surface area for a given mass of nanoparticles (Figure 11c, inset).

Online Detection Capability

A surfactant (e.g., 0.1 mg mL^{-1} Tween 20) is typically added to the WWC collection liquid to promote uniform particle dispersal in the liquid film and to enhance particle recovery with minimal foaming. These surfactants can influence Complexation interactions at the dye–nanoparticle interface in the microfluidic detection component, contributing to the enhancement or quenching of the fluorescence signature (Bielska, Sobczynska, & Prochaska, 2009). It is therefore essential to select surfactant and dye combinations that maintain uniform fluorescence without disrupting suspension stability (i.e., to avoid triggering aggregation and fouling of the microchannel). The data in Figure 13a show that Rose Bengal and Rhodamine 6G strongly interact with most

surfactants except those possessing like charges (e.g. SDS-Rose Bengal, CTAB-Rhodamine 6G), whereas the most severe complexation occurs when the surfactant and dye are oppositely charged (e.g. CTAB-Rose Bengal, SDS-Rhodamine 6G).

The combination of fluorescein dye with non-ionic Tween 20 and Tween 80 surfactants produces slight interfacial quenching that is beneficial from a detection standpoint because subsequent fluorescence enhancements can be straightforwardly attributed to the presence of nanoparticles.

Based on these results, we selected fluorescein dye for use in the microfluidic detection component to maintain compatibility with Tween 20 surfactant in the WWC collection liquid. Feasibility of operating the microfluidic detection component under conditions compatible with the WWC collector was assessed using standard test suspensions of ultrafine Al_2O_3 nanoparticles (average particle size ~100 nm). Interfacial fluorescence is strongest at low flow rates owing to the prolonged residence time within the microchannel that enables enhanced mixing by lateral diffusion between the co-flowing dye and nanoparticle streams (Figure 13b) (Atencia & Beebe, 2005). The fluidic output from the WWC collector is delivered at flow rates in the range of 0.04–0.2 mL min^{-1}, inherently ensuring pronounced fluorescence enhancement while avoiding particle sedimentation and deposition that could arise inside the microchannel in extremely slow flows. Interfacial fluorescence of the nanoparticles initially increases then decreases with Tween 20 concentration, displaying a maximum in the vicinity of 1.5 mg mL^{-1} (Figure 13c). This optimal Tween 20 concentration, however, is higher than the range of 0.1 mg mL^{-1} typically added to the WWC collection liquid. We

therefore chose to maintain the 0.1 mg mL^{-1} concentration in subsequent experiments to maximize compatibility with standard WWC operating conditions.

Collection and Analysis of Airborne Environmental Nanoparticles

We first established a correlation between interfacial fluorescence intensity and nanoparticle concentration using serial dilutions of a standard Al_2O_3 test suspension under conditions compatible with WWC operation (Figure 14a). An approximately linear-relationship is maintained at concentrations up to 1.0 and 1.2 wt% at flow rates of 0.2 and 0.02 mL min^{-1}, respectively, with fluorescence becoming saturated at higher concentrations. Interfacial fluorescence is enhanced at slower flow rates, yielding a detection limit of ~0.02 wt% at 0.02 mL min^{-1} in the ultrafine particle size range.

Next, we demonstrated integrated sampling and detection using the low cutpoint WWC to collect airborne Al_2O_3 nanoparticles aerosolized from our test suspensions and dispersed into an environmental chamber (Figure 14b). Sampling was performed at a 200 L min^{-1} air inflow rate ($\Delta p = 30'' H_2O$, 71% collection efficiency relative to dry filter control), and the WWC collection liquid containing the sampled nanoparticles was then co-injected into a microchannel in parallel with a 0.033 mg mL^{-1} fluorescein solution. We used a scanning mobility particle sizer (SMPS) to quantify the concentration and size distribution of aerosolized nanoparticles inside the test chamber, enabling a correlation to be established between interfacial fluorescence intensity and environmental nanoparticle concentration (Figure 14c). Mass concentrations were determined using the count concentration as a function of particle diameter from SMPS and a spherical particle density.

These results indicate that the microfluidic approach is capable of detecting Al_2O_3 nanoparticles in the ultrafine size range (4–160 nm) at airborne environmental concentrations below 200 μg m^{-3}, within established toxicity limits (e.g., NIOSH currently recommends a REL of 0.3 mg m^{-3} for "ultrafine" titanium dioxide as time-weighted average (TWA) for up to 10 h per day during a 40 h workweek, and 2.4 mg m^{-3} for "fine" TiO_2) (US National Institue for Occupational Safety and Health (NIOSH), 2011). We remark that our rationale for comparison with TiO_2 exposure standards (conventionally expressed in terms of mass concentration) is motivated by the fact that there are currently no broadly accepted hazard limits for nanosize Al_2O_3, despite mounting evidence of adverse health effects (Braydich-Stolle et al., 2010; Y. X. Li et al., 2012; Win-Shwe & Fujimaki, 2011). This deficiency reflects the current lack of exposure data needed to establish meaningful toxicity limits for even the most common nanomaterials – precisely the kind of information our technology can provide.

The fluorescence images in Figure 14c display features nearly identical to those observed in the standard test suspension (e.g., distinct enhancement in interfacial fluorescence bracketed by an adjacent depletion zone, see Figure 14a), indicating that the suspension's ultrafine particle size distribution is not significantly altered by aerosolization or collection. To further validate this conclusion, nanoparticles dispersed in the test chamber were characterized prior to WWC collection using SMPS (sub-150 nm ultrafine range) and aerodynamic particle sizing (APS, 0.5–20 μm range), and nanoparticles dispersed in the collection liquid after passing through the WWC were characterized using nanoparticle tracking analysis (NTA). The SMPS and NTA data

confirm that the ultrafine size distribution is not appreciably altered by aerosolization or WWC collection, while the APS data display no evidence that larger agglomerates were formed during aerosolization (Figure 14d). The geometric mean and geometric standard deviation of the size distributions obtained were 122.1 nm and 1.296 for SMPS and 128.2 nm and 1.210 for NTA, respectively, verifying that comparable particle sizes were obtained by each instrument before and after WWC collection.

Conclusion

The approach presented here demonstrates proof of concept for a compelling new capability to enable rapid monitoring, especially in occupational settings where elevated exposure to airborne nanomaterials fitting within an established compositional profile is of particular concern. Comparable throughput is challenging to obtain using current-generation personal samplers because materials must be collected over at least a full workday, thereby delivering a limited static view of a much larger dynamically evolving exposure profile. Our method enables quick readings to be sensitively obtained over volumes ranging from personal space (e.g., the 200 L min^{-1} flow rate we employed can probe a standard 30 L volume in under 10 s) to production floor scale. High flow rates can be used for rapid burst collections; low flow rates can be used for sampling in an "always on" state. Noise levels are comparable to a hair dryer operating at low speed. In addition to providing previously unavailable dynamic data needed to rationally establish safe exposure limits (e.g., to quantify transient exposure associated with movement of workers throughout the space), continuous monitoring can enable the source of a potentially hazardous release to be quickly pinpointed so that it can be mitigated before

posing a health risk. Sensitivity can be further enhanced (by at least an order of magnitude) through incorporation of an online pre-concentrator with virtually no loss of throughput. The microfluidic analysis format offers further advantages because it is inherently amenable for automation and scalable for high-throughput parallel operation. Additional functionality can be readily incorporated by exploiting the rich toolbox of mature particle fractionation approaches already demonstrated to function in the flow rate range of interest here (Pamme, 2007). Continuous separations can be performed across a broad range of particle size (e.g., by employing methods such as deterministic lateral displacement (L. R. Huang, Cox, Austin, & Sturm, 2004), inertial force (Di Carlo, Irimia, Tompkins, & Toner, 2007; J. H. Huang, Jayaraman, & Ugaz, 2012), pinched flow fractionation (Takagi, Yamada, Yasuda, & Seki, 2005), etc.) to enable upstream pre-fractionation (e.g., selective removal of larger particles, real-time size distribution characterization) and/or downstream enrichment and harvesting. The selective and reproducible nature of the underlying chemical and physical interactions between the nanoparticles and tracer dye (i.e., analogous to biological antibody–antigen interactions) also introduces the potential to obtain more detailed exposure profiles (nanoparticle composition, size range, surface area, etc.), establish "fingerprint" libraries of fluorescence signatures from multispecies mixtures, and permit analysis of biological materials.

CHAPTER V

SIMPLE ELECTRICAL CONDUCTIVITY MEASUREMENT FOR CONTINUOUS TIO_2 SYNTHESIS VIA MICROFLUIDICS

Continuous TiO_2 Synthesis and Detection via Microfluidics

Nanoparticle synthesis and manufacturing has become immensely important, both commercially and scientifically, as an increasingly broad range of products rely on nanomaterials to achieve enhanced performance and functionality (deMello, 2006; Lenshof & Laurell, 2010; Richman & Hutchison, 2009). Small-batch or microfluidic-based processing strategies are of particular interest owing to their ability to operate in a continuous format that delivers exquisite control over synthesis conditions via precise regulation of parameters such as flow rate / residence time, temperature, and reagent composition (Cottam et al., 2007; Dendukuri & Doyle, 2009; Jahn et al., 2008; Kenis et al., 1999; Krishna, Li, Li, & Kumar, 2013; Pumera, 2011; Song, Hormes, & Kumar, 2008; H. Z. Wang et al., 2004). But, continuous synthesis also requires availability of online monitoring and characterization tools to ensure that the generated products consistently display optimal properties for the target application (Richman & Hutchison, 2009). Measurement of the suspension's bulk electrical conductivity (EC) offers an attractive pathway to achieve this goal, particularly in the case of oxide nanoparticles whose charged surface groups inherently generate size- and composition-dependent electrical signatures (Cruz, Reinshagen, Oberacker, Segadaes, & Hoffmann, 2005; Kang

& Li, 2009; Obrien, 1981; Roa, Carrique, & Ruiz-Reina, 2011; Sarojini, Manoj, Singh, Pradeep, & Das, 2013; Sigmund, Bell, & Bergstrom, 2000; Vahey & Voldman, 2009).

Impedance-based methods under application of an alternating current have been the predominant avenue used to perform liquid phase EC measurements (Collins & Lee, 2004; Bruce K. Gale, Caldwell, & Frazier, 1998; Hatsuki, Yujiro, & Yamamoto, 2013; Justin, Nasir, & Ligler, 2011), This approach has been successfully miniaturized and applied in microfluidic systems to detect, separate, and manipulate alkali metal ions (Guijt et al., 2001), cells (Beck, Shang, Marcus, & Hamers, 2005), nanoparticles (Fraikin, Teesalu, McKenney, Ruoslahti, & Cleland, 2011), microcapsules (Sun, Bernabini, & Morgan, 2009) and viruses (Patolsky et al., 2004). Cyclic voltammetry has also been employed at the microscale to detect DNA hybridization (Marchand, Delattre, Campagnolo, Pouteau, & Ginot, 2005) and to monitor Ag wire synthesis (Kenis et al., 1999). These methods require precise micro- or nano-patterning of electrode arrays via photolithography and LIGA-based methods to achieve the small inter-electrode spacings necessary for optimal impedance measurement (Galloway et al., 2002). Although device fabrication is generally straightforward, the need for specialized facilities to produce these features has limited widespread adoption of these technologies because it is challenging to an economy of scale that would make them cost effective. Another important limitation involves the equipment needed to acquire and analyze the impedance data. The typical workflow is carried out in a dedicated laboratory setting using precision instruments, with offline data processing carried out on a computer workstation. This lack of portability limits the ability to perform on site measurements,

introducing uncertainties associated with potential changes in the state of the nanomaterial suspension that may occur between the time it is sampled and the time during which it is transported the lab for analysis. Rapid characterization is also highly desirable from the standpoint of enabling real-time feedback and control of process conditions to support continuous manufacturing and quality control. In this paper, we introduce an approach that addresses both of these shortcomings by leveraging a simplified electrode patterning method and DC-based analysis methodology to perform rapid EC characterization of nanoparticle size and composition in suspension using inexpensive consumer-class digital multimeters.

To consider the simple electrode preparation, printed circuit board (PCB) is an inexpensive and straightforward technique to fabricate electronic patterns. It was combined with disposable biochip as an electronic reading apparatus, to perform contactless electrical impedance measurements yet has not been further investigated as integrated fabrication containing electrodes (Emaminejad, Javanmard, Dutton, & Davis, 2012). Few work explored to print electrodes patterns without sacrifice layer by using of pre-printed wax paper (Cho et al., 2007; Paixao & Bertotti, 2009; Tang, Vaze, & Rusling, 2012; Yu, Li, & Ou, 2012), which will be helpful to reduce manufacturing cost and time. To think about the data acquiring method, several work reported voltage-current characteristics in microfluidic reactors to enable continuous producing and monitoring of the liquid flow rates during micro-reactor operation (Fletcher, Haswell, & Zhang, 2001), to probe germination spores in microfluidic biochips (Y. S. Liu et al., 2007), and to measure ion transport in nanofluidic funnels (Perry, Zhou, Harms, & Jacobson, 2010).

These voltage-current characteristics could be completed by commercial LCR meters. A electrical conductivity (EC)-based method for fluidic resistance measurement is reported as a useful tool for static or real-time characterization of microfluidic systems (Godwin, Deal, Hoepfner, Jackson, & Easley, 2013). This measurement applying direct current (DC) and could be facilitated by a standard voltage meter. They measured the electrical resistance of a channel filled with a conductivity standard solution to directly correlate to the fluidic resistance, which is analogous to resistance measurements in electrical circuits

It is well known oxide nanoparticles, when dissolved into water or other liquid, will contribute to bulk electrical conductivity (EC) (Kang & Li, 2009; Sigmund et al., 2000). Because their surface group and the ion buried in EDL can vary with particle size, and apparently their content decide total charges, the EC would disclose these decisive parameters. Several works have investigated relationship of the EC of nanoparticle suspension with or without electrolyte (Cruz et al., 2005; Obrien, 1981; Roa et al., 2011; Sarojini et al., 2013). A example to use these correlation is for high-throughput cell and particle (Vahey & Voldman, 2009). However, few works apply the EC of nanoparticle suspension to monitor nanoparticle suspension during continuous synthesis via microfluidics.

Several ways can be used to do electrical detection. Current popular conductivity detectors are using alternative current (Justin et al., 2011) to avoid complicated diode-like effect occurring in electrode/fluidic interface. Alkali metal ions (Guijt et al., 2001), cells (Beck et al., 2005), nanoparticles (Fraikin et al., 2011), microcapsules (Sun et al.,

2009) and viruses (Patolsky et al., 2004) can be effectively detected, separated or manipulated by impedance or admittance (Collins & Lee, 2004) signal in this way. Contactless impedance flow cytometry has also been introduced (Emaminejad et al., 2012). These, however, require fabricating electrodes in dedicate manner to reduce the distance between them. Photoresist and LIGA techniques were mostly used, which are effective but intricate and involve toxicity (Galloway et al., 2002) as well. Cyclic voltammeter can be used to detect DNA hybridization (Marchand et al., 2005) or Ag wire microfabriaction (Kenis et al., 1999). Recent work successfully used DC to measure voltage-current characteristics of a micro-reactor channel network (Fletcher et al., 2001) and germination of miable model Bacillus anthracis pores in microfluidic biochips (Y. S. Liu et al., 2007). Microchannel fluidic resistance was recently measured with a standard voltage meter (Godwin et al., 2013) and linear correlation of potential to current has been observed on the resistance of axis fluid segment (Perry et al., 2010), offering a simple way for real-time characterization of microfluidic systems.

In this paper, we introduce an approach that addresses both of these shortcomings by leveraging a simplified electrode patterning method and DC-based analysis methodology to perform rapid EC characterization of nanoparticle size and composition in suspension using inexpensive consumer-class digital multimeters (Figure 3).

Electrical Conductivity Reveals Nanoparticle Suspension Information

Previous studies involving oxide-based nanoparticle suspensions have established that bulk electrical conductivity is proportional to the particle concentration in suspension (Chakraborty & Padhy, 2008; E. Lee, Chih, & Hsu, 2001). These effects

are generally interpreted in terms of a framework based on particles' electrical double layer (EDL), where an interplay exists between increased counterion capacity (acting to increase conductivity as the EDL thickness increases) and reduced electrophoretic mobility (acting to decrease conductivity as the EDL thickness increases) (Ban, Lin, & Song, 2010; Chakraborty & Padhy, 2008; Das & Chakraborty, 2010; Roa et al., 2011). We examined bulk suspensions of TiO_2 and ZnO nanoparticles, and observed that their electrical conductivity (EC) increases with nanoparticle concentration in agreement with previous literature (Fig. 15b and b) (Cruz et al., 2005; Ganguly, Sikdar, & Basu, 2009; Sarojini et al., 2013). We measured these samples' EC in batch (Materials and Methods) and the linear fits to these data (Figure. 15, and 16 and Table 8) therefore make it possible to establish a mapping between suspension conductivity, and particle size or concentration. Our goal, then, is to determine how to relate DC-based conductivity measurements obtained in the microfluidic device to these corresponding quantities obtained in bulk suspensions.

Circuit Model for Measurement

We begin by noting that the measurement circuit embeds contributions from the nanoparticle suspension and the electrode-fluid interfaces (Figure. 15c) (Jakoby & Vellekoop, 2011), whereas the suspension electrical conductivity is governed by contributions from the surface charge of the particles and the electrolytes (Palkar & Schure, 1997). When a DC potential is applied between electrodes in contact with the suspension, the measured resistance ($R_{measured}$) embeds combined contributions from the fluid (R_{fluid}) and the electrode-fluid interfaces. Charge-transfer at the electrode-fluid

interface is governed by electrochemical processes (Schoch, Han, & Renaud, 2008) that can be expressed in terms of an electrode/fluid interface capacitance, a charge-transfer resistance (R_{ct}) that varies with the fluid's conductivity, and an impedance (typically referred to as a constant phase element (*CPE*) that accounts for the onset of diffusion limited electrochemistry under high applied potentials. Since our measurement approach involves application of relatively small potentials (the same order of 1 V), the *CPE* only contributes minimally to the overall resistance. Furthermore, since we consider only direct current potentials, all capacitances can be ignored yielding $R_{measured} = R_{ct} + CPE + R_{fluid}$. We can therefore group R_{ct} and CPE into a single "black box" resistance term ($R_{black\ box} = R_{ct} + CPE$), resulting in the following expression for the measured resistance $R_{measured} = R_{black\ box} + R_{fluid}$.

There are two possible ways to utilize our micro device for the nanoparticles measurement (Figure. 3d). Apparently, the right method requires pre-calculated $R_{black\ box}$ and pre-established mapping between suspension conductivity and particle size or concentration to be incorporated into decoding the information of measured samples, and will consequently avoid the calibration step during the sample measurement procedure. This is going to be helpful to achieve rapid and straightforward operation during application compared with the left procedure which needs calibration by using of specific standards.

We used KCl solutions of known conductivity to determine the value of the "black box" resistance term $R_{measured,\ KCL} = R_{black\ box} + R_{fluid,\ KCL}$, where $R_{fluid,\ KCL}$ is obtained from bulk EC measurements of KCl solution conductivity and knowledge of

the microchannel cross sectional area A and distance between electrodes L via $R_{fluid,\,KCL} = EC_{KCl}$ x L / A (Figure. 4a-c). Comparing measurements obtained in microchannel segments of different length (red and blue dots), it can be seen that that longer segments and smaller cross sectional areas reduce the contribution of $R_{black\ box}$, whereas wider electrodes do not significantly affect the measurement, consistent with the above framework. The resistance model is independent of flow rate (B. K. Gale, Caldwell, & Frazier, 2002).

These value is later used to determine the corresponding fluid resistance in the microchannel. By subtracting $R_{black\ box}$ from correlation to LRC meter measured $R_{measured}$ of TiO_2 samples, we could find the resistance of fluid R_{fluid} and consequently the bulk electrical conductivity (EC) of fluid based on $EC_{sample} = R_{fluid,\,sample}$ x A / L.

Since we have linear fitting of the bulk EC of TiO_2 to the concentration by Figure 15a, b and 16, the concentration for TiO_2 suspension in each test is able to be captured. We compare the calculated contents of TiO_2 based on resistance measurement via microfluidic with the actual concentrations we prepared in Figure. 17d-f. According to the result, among assorted designs, smaller channel height (around 40 μm) is favorable to give best fitting between measured values and actual values. Then we used the optimized design for continuous synthesis and quality control of nano-sized TiO_2.

Online Detection for TiO_2 Synthesis

The TiO_2 nanoparticles are synthesized in the channel by well-known hydrolysis of titanium tetraisoproxide (TTIP) using a Y-shape channel to mix dispersed TTIP and dispersed DI water. The hydrolysis is very fast and white flocculent particles were

observed inside microchannel. Figure 18a show the size of produced particles main around 10 nm under SEM images, however it may slightly increase when more concentrated TTIP added in continuous synthesis. Since we use IPA to disperse all the reagents and products and thus the whole fluid is much less conductive then aqueous suspension for electrical measurement, we added some strong electrolytes (KCl) to increase the sensitivity for our measurement. When electrolytes exist, adding particles will reduce the electrical conductivity of suspension and alike correlation has been explored by previous work. (Cruz et al., 2005) The measured segment resistances were processed to give corresponding fluid EC. Based on the correlating of EC to TiO_2 content by batch measurement (Figure 19), we could read the content of TiO_2. The ECs measured via microchannel match well with those measured via batch and the TiO_2 contents match well with the actually prepared suspensions as shown in Figure 18b

Nanoparticle concentration measurement in microfluidic device here is based on the overlap of area that dissolved oxide nanoparticles into water or other liquid will contribute to electrical conductivity (EC) in suspension and this electrical conductivity can be directed measured by simply fabricated microfluidic device in DC current. The conventional way to deposit metal electrodes need photoresist and lift-off soft lithograph. Alternatively, we used a heat-and-press film to transfer printed pattern in copper onto glass slide (Cho et al., 2007). In contrast to photolithography method for nanofabrication, our protocol does not require expensive instrumentation nor photoresist as a sacrifice layer.

The Circuit model for our approach to measure follow resistance inside microchannel suggests "Black Box Resistance" ($R_{black\ box}$) need to be obtain before nanoparticle measurement. This $R_{\text{Black Box}}$ values will change based on device geometry such as the channel height and electrodes width and gap (Figure 17a-c). These values could be calibrated routinely by standards and assumed well corresponding to controllable feature quality of microfluidic device during practical manufacturing and application in the future. By comparing the calculated TiO_2 contents with the actual TiO_2 contents prepared by dissolving powder into DI water based on EC measurement (Figure 17d-f), a nice match could be achieved to verify our measurement of nanoparticle concentration via microfluidic device. Generally, smaller channel height could help to main better agreement between actual and measured values.

The measured electrical conductivity and TiO_2 via microfluidic device both show nice matching with the conventional batch measurement or actual values at online mode. The TTIP dosage slightly changed the sizes of the synthesized particles (Figure 18a) but certainly produce quite various concentrated TiO_2, so it is safely to infer the measured resistance will reveal the particle concentrations in these continuously synthesized nanofluids. To control the reaction and product concentration, dispersant such as IPA was added into the reagents. This will dilute the produced nanoparticle concentration and result in much smaller EC of the nanofluids. We also added KCl as the strong electrolytes to increase the sensitivity for electrical measurement via our microchannel device. Screening appropriate dispersant and electrolytes (if necessary) to control satisfactory reaction and conductivity will be an important topic to fulfill the electrical

measurement during continuous synthesis inside microchannel. That is, more diluted reactive reagents (e.g. TTIP) will reduce the risk of fouling in the channel; however decrease the producing capacity and resistance measurement sensitivity. And more electrolytes will increase the conductivity but enhance the separation and rinsing work. In the case that produced particles are highly conductive or concentrated, electrolytes adding is not necessary. Considering many works reported to enable controlling the size of nanoparticle under microfluidic continuous synthesis approach, it is possible to integrate this simply fabricated device for a quick concentration measurement. Slight bigger instability of the correlation profiles (Figure 18b) was displayed during synthesis process compared with those profiles (Figure 17d-f) from suspensions prepared by commercial powders. This is probably due to the slight fluctuation of flow or concentration distribution in span of the whole mixing and heterogeneous reacting procedure.

Offline Detection of Nanoparticle Suspension

Moreover, the electrode inserted microchannel can also be applied for offline detection. In this case, micro liter sample is enough for one single measurement, as long as segment between electrodes could be fully filled (Figure 20a), while conventional EC meter demand much larger volume sample (~20mL) to ensure the probe could totally immerse into the sample solution. We used pipette to inject series KCl solutions into microchannel to measure the corresponding correlation of $R_{\mathrm{Black\ Box}}$ to measured resistance R_{measured}. (Figure 20b). Notably, a cheaper multimeter was used instead of Keithley LCR meter to measure the segment electrical resistance, proving our device

could offer meaningful results when combined with economical instrument to enable a low cost way to determine the nanoparticle concentration inside suspension. The measured resistance data is used to calculate fluid resistance values based on equations above, which are compared with calculated fluid resistance based on batch measured electrical conductivity and channel geometry (Figure 20b). Remarkably, when the microchannel device is used under offline mode, since the fluid is not under steady state without passive force and ions accumulate among electrodes without convective flow refreshing. Moreover, when stopping injecting the sample into micro device, a small jump may occur (Figure 20a). All these make the measured results fluctuated more than the continuous mode (Figure 20b, 20c) and the microchannel has less service life. A novel improvement of the electrode will help to obtain better results and measurement ability based our device design and use.

The proposed detection method, together with straightforward and swift fabrication techniques, potentially enables the detection system to be portable, automated for nanoparticle synthesis. Moreover, the proposed approach can be applied to determine viability of the interface synthesis in microchannel. Reaction kinetics can also be investigated by this detection method.

CHAPTER VI

CONCLUDING REMARKS

Nanoparticle characterization is immensely important owing to the increasing significance of these materials in areas such as photovoltaics, catalysis, and sensors. Many of these applications involve suspension-based synthesis and processing of nanoparticles in suspension, and demand precise control of properties such as chemistry, size, morphology and/or crystalline structure to achieve desired functionalities and performance. Unfortunately, current-generation characterization methods have generally failed to keep up with this rapid pace of discovery, introducing a significant bottleneck between scientific development and commercialization of nanomaterial-based products. This research has focused on development of novel approaches that overcome limitations of conventional analysis methods, enabling continuous online quantification and characterization of nanoparticle composition, size, and morphology, independent of agglomeration state. Our microfluidic approach enables real-time and continuous analysis by exploiting localized fluorescent complexation of nanoparticles in suspension, yielding a signature easily detectable over a broad concentration range. In Chapter III, we evaluated our approach by co-injecting fluorescein dye into a microchannel in parallel with suspensions of ZnO and TiO_2 (anatase and rutile) nanoparticles. The speed and simplicity of this method offers compelling advantages for routine compositional monitoring in nano manufacturing settings. Our method can also be readily applied to establish fluorescence signature fingerprints of complex (and more realistic) suspension-

based nanomaterial products incorporating coatings and stabilizing additives. Few other approaches are able to instantaneously deliver this kind of quantitative characterization in an online format, suggesting broad applicability as a routine tool that can supplement the workhorse analytical methods in a host of emerging manufacturing settings.

We also formulated a reaction-diffusion model in Chapter III, applied it to verify experimental findings and capture the fundamental underlying transport and adsorption phenomena. The computational model enables the fluorescence signature to be correlated with particle size, and can be further refined to enable characterization of mixtures containing different particle species (e.g., anatase and rutile TiO_2).

In Chapter IV, we demonstrated proof of concept for a compelling new capability to enable rapid monitoring, especially in occupational settings where elevated exposure to airborne nanomaterials fitting within an established compositional profile is of particular concern. We achieved comparable throughput to obtain using current-generation personal samplers to enable collecting materials over at least a full workday, thereby delivering a capable static view of a much larger dynamically evolving exposure profile. High flow rates can be used for rapid burst collections; low flow rates can be used for sampling in an "always on" state, making it capable of quick readings to be sensitively obtained over volumes ranging from personal space to production floor scale. Our approach can provide previously unavailable dynamic data needed to rationally establish safe exposure limits, such as to quantify transient exposure associated with movement of workers throughout the space. Additionally, our continuous monitoring can enable the source of a potentially hazardous release to be quickly pinpointed so that

it can be mitigated before posing a health risk. The sensitivity is more related to the microfluidic device and it can be further enhanced (by at least an order of magnitude) through incorporation of an online pre-concentrator with virtually no loss of throughput. The microfluidic platform is also highly scalable, offering considerable potential for automation via high-throughput parallel operation. Additional functionality can be readily incorporated by exploiting the diverse toolbox of mature particle fractionation approaches already demonstrated to function in the flow rate range of interest here.

Integration with other instruments to deliver broader functionality is an area for future improvement. Continuous separations across a broad range of particle size, for example, can enable upstream pre-fractionation and/or downstream enrichment and harvesting (Pamme, 2007). Methods such as deterministic lateral displacement (L. R. Huang et al., 2004), inertial force (Di Carlo et al., 2007), and pinched flow fractionation (Takagi et al., 2005) can help to achieve selective removal of larger particles, real-time size distribution characterization. Characterization of more complex mixtures and nano-scale biological species with specific surface receptor sites can be enabled by establishing libraries of fluorescence signature "fingerprints". The selective and reproducible nature of the underlying chemical and physical interactions between the nanoparticles and tracer species (i.e., analogous to biological antibody–antigen interactions) also introduces the potential to obtain more detailed exposure profiles (nanoparticle composition, size range, surface area, etc.).

In addition to continuous environmental monitoring, our analysis format supports real-time characterization of solution-based nanomaterials customarily employed as

additives and coatings owing to its inherent ability to performance in a portable and automated manner. In Chapter V, we explore this possibility by demonstrating characterization of nanoparticle suspensions via DC electrical conductivity measurements in a simply fabricated microfluidic format. Conventional fabrication methods require cleanroom processing to pattern metal electrodes. We eliminate these complexities by employing a thermal transfer film to construct copper electrodes on glass slide substrates (Cho et al., 2007). In contrast to conventional photolithography, our method does not require expensive equipment or photoresist-based processing.

We have developed a circuit model to describe our approach that, when combined with routine standards-based calibration, enables accurate on-line material characterization. Good accuracy is achievable in TiO_2 nanoparticle suspensions regardless of whether an online or offline sampling mode is employed. Adaptation to continuous monitoring of nanoparticle synthesis requires some considerations for optimal characterization results. For example, dispersants such as IPA that are typically added to control the reaction and product concentration may dilute the produced nanoparticle concentration and result in a much smaller conductivity signal. We dealt with this by adding KCl to increase measurement sensitivity. Therefore, screening of appropriate dispersants and/or electrolytes to control the reaction while delivering sufficient conductivity for online measurement will be an important topic for future study to apply our method for monitoring continuous synthesis. There is also a tradeoff between over-dilution of reactive reagents (e.g. TTIP) to reduce fouling in the channel while maintaining sufficient production capacity and resistance measurement sensitivity.

Similarly, addition of more electrolyte increases conductivity but may also require additional post-synthesis purification. In cases where particles are highly conductive or concentrated, however, addition of more electrolytes is not necessary. Alternative electrode configurations such as enlarged cross area of microchannel and shorter segment lengths between electrodes can also be considered to improve performance.

A comparison of this work to existing nanoparticle characterization methods is provided in Table 9. Our method is is uniquely sensitive to low-density materials and aggregates, and can also handle non-spherical particles. The measured particle size range we have explored here is as small as 40 nm in fluorescence experiments and 10 nm in the online synthesis with electric conductivity measurements. But there is also considerable potential to extend this to smaller particle sized by employing tracer species with more sensitive and/or specific interactions.

Looking ahead, our approaches fit naturally with new efforts to develop rapid "on-demand" nanomaterial synthesis capabilities. There is also considerable potential for reaction kinetics to be rapidly extracted in combination with robust physico-chemical model-based control, laying the foundation for high-throughput screening that can have broad applicability as a convenient tool to probe chemical and biological interactions.

REFERENCES

Atencia, J., & Beebe, D. J. (2005). Controlled microfluidic interfaces. *Nature, 437*(7059), 648-655.

Auffan, M., Rose, J., Bottero, J. Y., et al. (2009). Towards a definition of inorganic nanoparticles from an environmental, health and safety perspective. *Nature Nanotechnology, 4*(10), 634-641.

Balbus, J. M., Maynard, A. D., Colvin, V. L., et al. (2007). Meeting report: Hazard assessment for nanoparticles - Report from an interdisciplinary workshop. *Environmental Health Perspectives, 115*(11), 1654-1659.

Ban, H., Lin, B. C., & Song, Z. R. (2010). Effect of electrical double layer on electric conductivity and pressure drop in a pressure-driven microchannel flow. *Biomicrofluidics, 4*(1), 13.

Batterman, S. A., Franzblau, A., D'Arcy, J. B., et al. (1998). Breath, urine, and blood measurements as biological exposure indices of short-term inhalation exposure to methanol. *International Archives of Occupational and Environmental Health, 71*(5), 325-335.

Beck, J. D., Shang, L., Marcus, M. S., et al. (2005). Manipulation and real-time electrical detection of individual bacterial cells at electrode junctions: A model for assembly of nanoscale biosystems. *Nano Letters, 5*(4), 777-781.

Bielska, M., Sobczynska, A., & Prochaska, K. (2009). Dye-surfactant interaction in aqueous solutions. *Dyes and Pigments, 80*(2), 201-205.

Bonner, J. C., Silva, R. M., Taylor, A. J., et al. (2013). Interlaboratory Evaluation of Rodent Pulmonary Responses to Engineered Nanomaterials: The NIEHS Nano GO Consortium. *Environmental Health Perspectives, 121*(6), 676-682.

Borm, P. Y. A., Costa, D., Castranova, V., et al. (2000). The relevance of the rat lung response to particle overload for human risk assessment: A workshop consensus report. *Inhalation Toxicology, 12*(1-2), 1-17.

Braydich-Stolle, L. K., Speshock, J. L., Castle, A., et al. (2010). Nanosized Aluminum Altered Immune Function. *Acs Nano, 4*(7), 3661-3670.

Cena, L. G., Anthony, T. R., & Peters, T. M. (2011). A Personal Nanoparticle Respiratory Deposition (NRD) Sampler. *Environmental Science & Technology, 45*(15), 6483-6490.

Chakraborty, S., & Padhy, S. (2008). Anomalous electrical conductivity of nanoscale colloidal suspensions. *Acs Nano, 2*(10), 2029-2036.

Cho, H. J., Parameswaran, M., & Yu, H. Z. (2007). Fabrication of microsensors using unmodified office in inkjet printers. *Sensors and Actuators B-Chemical, 123*(2), 749-756.

Collins, J., & Lee, A. P. (2004). Microfluidic flow transducer based on the measurement of electrical admittance. *Lab on a Chip, 4*(1), 7-10.

Cottam, B. F., Krishnadasan, S., deMello, A. J., et al. (2007). Accelerated synthesis of titanium oxide nanostructures using microfluidic chips. *Lab on a Chip, 7*(2), 167-169.

Cruz, R. C. D., Reinshagen, J., Oberacker, R., et al. (2005). Electrical conductivity and stability of concentrated aqueous alumina suspensions. *Journal of Colloid and Interface Science, 286*(2), 579-588.

Das, S., & Chakraborty, S. (2010). Effect of conductivity variations within the electric double layer on the streaming potential estimation in narrow fluidic confinements. *Langmuir, 26*(13), 11589-11596.

deMello, A. J. (2006). Control and detection of chemical reactions in microfluidic systems. *Nature, 442*(7101), 394-402.

Dendukuri, D., & Doyle, P. S. (2009). The synthesis and assembly of polymeric microparticles using microfluidics. *Advanced Materials, 21*(41), 4071-4086.

Dendukuri, D., Pregibon, D. C., Collins, J., et al. (2006). Continuous-flow lithography for high-throughput microparticle synthesis. *Nature Materials, 5*(5), 365-369.

Di Carlo, Dino, Irimia, Daniel, Tompkins, Ronald G., et al. (2007). Continuous inertial focusing, ordering, and separation of particles in microchannels. *Proceedings of the National Academy of Sciences of the United States of America, 104*(48), 18892-18897.

Duraiswamy, S., & Khan, S. A. (2010). Plasmonic Nanoshell Synthesis in Microfluidic Composite Foams. *Nano Letters, 10*(9), 3757-3763.

Emaminejad, S., Javanmard, M., Dutton, R. W., et al. (2012). Microfluidic diagnostic tool for the developing world: contactless impedance flow cytometry. *Lab on a Chip, 12*(21), 4499-4507.

Evans, D. E., Heitbrink, W. A., Slavin, T. J., et al. (2008). Ultrafine and respirable particles in an automotive grey iron foundry. *Annals of Occupational Hygiene, 52*(1), 9-21.

Fletcher, P. D. I., Haswell, S. J., & Zhang, X. L. (2001). Electrical currents and liquid flow rates in micro-reactors. *Lab on a Chip, 1*(2), 115-121.

Foley, Jennifer O., Nelson, Kjell E., Mashadi-Hossein, Afshin, et al. (2007). Concentration gradient immunoassay. 2. Computational modeling for analysis and optimization. *Analytical Chemistry, 79*(10), 3549-3553.

Fraikin, J. L., Teesalu, T., McKenney, C. M., et al. (2011). A high-throughput label-free nanoparticle analyser. *Nature Nanotechnology, 6*(5), 308-313.

Fujishima, A., Zhang, X. T., & Tryk, D. A. (2008). TiO2 photocatalysis and related surface phenomena. *Surface Science Reports, 63*(12), 515-582.

Funk, S., Hokkanen, B., Burghaus, U., et al. (2007). Unexpected adsorption of oxygen on TiO2 nanotube arrays: Influence of crystal structure. *Nano Letters, 7*(4), 1091-1094.

Gale, B. K., Caldwell, K. D., & Frazier, A. B. (2002). Geometric scaling effects in electrical field flow fractionation. 2. Experimental results. *Analytical Chemistry, 74*(5), 1024-1030.

Gale, Bruce K., Caldwell, Karin D., & Frazier, A. Bruno. (1998). Electrical conductivity particle detector for use in biological and chemical micro-analysis systems. *Proc. SPIE 3515, 3515*, 230-241.

Galloway, M., Stryjewski, W., Henry, A., et al. (2002). Contact conductivity detection in poly(methyl methacylate)-based microfluidic devices for analysis of mono- and polyanionic molecules. *Analytical Chemistry, 74*(10), 2407-2415.

Ganguly, S., Sikdar, S., & Basu, S. (2009). Experimental investigation of the effective electrical conductivity of aluminum oxide nanofluids. *Powder Technology, 196*(3), 326-330.

Gerloff, K., Fenoglio, I., Carella, E., et al. (2012). Distinctive Toxicity of TiO2 Rutile/Anatase Mixed Phase Nanoparticles on Caco-2 Cells. *Chemical Research in Toxicology, 25*(3), 646-655.

Godwin, L. A., Deal, K. S., Hoepfner, L. D., et al. (2013). Measurement of microchannel fluidic resistance with a standard voltage meter. *Analytica Chimica Acta, 758*, 101-107.

Grassian, V. H. (2008). When Size Really Matters: Size-Dependent Properties and Surface Chemistry of Metal and Metal Oxide Nanoparticles in Gas and Liquid Phase Environments. *Journal of Physical Chemistry C, 112*(47), 18303-18313.

Guijt, R. M., Baltussen, E., van der Steen, G., et al. (2001). New approaches for fabrication of microfluidic capillary electrophoresis devices with on-chip conductivity detection. *Electrophoresis, 22*(2), 235-241.

Hardin, B. E., Snaith, H. J., & McGehee, M. D. (2012). The renaissance of dye-sensitized solar cells. *Nature Photonics, 6*(3), 162-169.

Hata, M., Thongyen, T., Bao, L., et al. (2013). Development of a high-volume air sampler for nanoparticles. *Environmental Science: Processes & Impacts, 15*(2), 454-462.

Hatch, A., Garcia, E., & Yager, P. (2004). Diffusion-based analysis of molecular interactions in microfluidic devices. *Proceedings of the Ieee, 92*(1), 126-139.

Hatch, A., Kamholz, A. E., Hawkins, K. R., et al. (2001). A rapid diffusion immunoassay in a T-sensor. *Nature Biotechnology, 19*(5), 461-465.

Hatsuki, R., Yujiro, F., & Yamamoto, T. (2013). Direct measurement of electric double layer in a nanochannel by electrical impedance spectroscopy. *Microfluidics and Nanofluidics, 14*(6), 983-988.

Heitbrink, W. A., Evans, D. E., Ku, B. K., et al. (2009). Relationships Among Particle Number, Surface Area, and Respirable Mass Concentrations in Automotive Engine Manufacturing. *Journal of Occupational and Environmental Hygiene, 6*(1), 19-31.

Hext, P. M., Tomenson, J. A., & Thompson, P. (2005). Titanium dioxide: Inhalation toxicology and epidemiology. *Annals of Occupational Hygiene, 49*(6), 461-472.

Holder, Amara L., Vejerano, Eric P., Zhou, Xinzhe, et al. (2013). Nanomaterial disposal by incineration. *Environmental Science: Processes & Impacts, 15*(9), 1652-1664.

Hong, S. B., Kim, D. S., Ryu, S. Y., et al. (2009). Design and Testing of a Semi-Continuous Measurement System for Ionic Species in PM2.5. *Particle & Particle Systems Characterization, 25*(5-6), 444-453.

Hu, S. S., & McFarland, A. R. (2007). Numerical performance simulation of a wetted wall bioaerosol sampling cyclone. *Aerosol Science and Technology, 41*(2), 160-168.

Huang, J. H., Jayaraman, A., & Ugaz, V. M. (2012). Enzymatic Sculpting of Nanoscale and Microscale Surface Topographies. *Angewandte Chemie-International Edition, 51*(38), 9619-9623.

Huang, L. R., Cox, E. C., Austin, R. H., et al. (2004). Continuous particle separation through deterministic lateral displacement. *Science, 304*(5673), 987-990.

Jahn, A., Reiner, J. E., Vreeland, W. N., et al. (2008). Preparation of nanoparticles by continuous-flow microfluidics. *Journal of Nanoparticle Research, 10*(6), 925-934.

Jakoby, B., & Vellekoop, M. J. (2011). Physical sensors for liquid properties. *Ieee Sensors Journal, 11*(12), 3076-3085.

Jeong, C. H., & Evans, G. J. (2009). Inter-Comparison of a Fast Mobility Particle Sizer and a Scanning Mobility Particle Sizer Incorporating an Ultrafine Water-Based Condensation Particle Counter. *Aerosol Science and Technology, 43*(4), 364-373.

The Joint Research Centre of the European Commission. (2012). Requirements on Measurements for the Implementation of the European Commission Definition of the Term "Nanomaterial".

Justin, G., Nasir, M., & Ligler, F. S. (2011). Hydrodynamic and electrical considerations in the design of a four-electrode impedance-based microfluidic device. *Analytical and Bioanalytical Chemistry, 400*(5), 1347-1358.

Justino, C. I. L., Rocha-Santos, T. A., & Duarte, A. C. (2011). Sampling and characterization of nanoaerosols in different environments. *Trac-Trends in Analytical Chemistry, 30*(3), 554-567.

Kamholz, A. E., Weigl, B. H., Finlayson, B. A., et al. (1999). Quantitative analysis of molecular interaction in a microfluidic channel: The T-sensor. *Analytical Chemistry, 71*(23), 5340-5347.

Kang, Y. J., & Li, D. Q. (2009). Electrokinetic motion of particles and cells in microchannels. *Microfluidics and Nanofluidics, 6*(4), 431-460.

Karakoti, A. S., Hench, L. L., & Seal, S. (2006). The potential toxicity of nanomaterials - The role of surfaces. *Jom, 58*(7), 77-82.

Kathiravan, A., Chandramohan, M., Renganathan, R., et al. (2009). Cyanobacterial chlorophyll as a sensitizer for colloidal TiO2. *Spectrochimica Acta Part a-Molecular and Biomolecular Spectroscopy, 71*(5), 1783-1787.

Kenis, P. J. A., Ismagilov, R. F., & Whitesides, G. M. (1999). Microfabrication inside capillaries using multiphase laminar flow patterning. *Science, 285*(5424), 83-85.

Khan, S. A., & Jensen, K. F. (2007). Microfluidic synthesis of titania shells on colloidal silica. *Advanced Materials, 19*(18), 2556-+.

Khlystov, A., Wyers, G. P., & Slanina, J. (1995). THE STEAM-JET AEROSOL COLLECTOR. *Atmospheric Environment, 29*(17), 2229-2234.

Kim, S., & Ehrman, S. H. (2009). Photocatalytic activity of a surface-modified anatase and rutile titania nanoparticle mixture. *Journal of Colloid and Interface Science, 338*(1), 304-307.

Krishna, K. S., Li, Y. H., Li, S. N., et al. (2013). Lab-on-a-chip synthesis of inorganic nanomaterials and quantum dots for biomedical applications. *Advanced Drug Delivery Reviews, 65*(11-12), 1470-1495.

Lee, B. P., Li, Y. J., Flagan, R. C., et al. (2013). Sizing Characterization of the Fast-Mobility Particle Sizer (FMPS) Against SMPS and HR-ToF-AMS. *Aerosol Science and Technology, 47*(9), 1030-1037.

Lee, E., Chih, M. H., & Hsu, J. P. (2001). Conductivity of a concentrated spherical colloidal dispersion. *Journal of Physical Chemistry B, 105*(4), 747-753.

Lenshof, A., & Laurell, T. (2010). Continuous separation of cells and particles in microfluidic systems. *Chemical Society Reviews, 39*(3), 1203-1217.

Li, G. H., Richter, C. P., Milot, R. L., et al. (2009). Synergistic effect between anatase and rutile TiO2 nanoparticles in dye-sensitized solar cells. *Dalton Transactions*(45), 10078-10085.

Li, M., Schnablegger, H., & Mann, S. (1999). Coupled synthesis and self-assembly of nanoparticles to give structures with controlled organization. *Nature, 402*(6760), 393-395.

Li, Y. X., Yu, S. H., Wu, Q. L., et al. (2012). Chronic Al2O3-nanoparticle exposure causes neurotoxic effects on locomotion behaviors by inducing severe ROS production and disruption of ROS defense mechanisms in nematode Caenorhabditis elegans. *Journal of Hazardous Materials, 219*, 221-230.

Liou, S. H., Tsou, T. C., Wang, S. L., et al. (2012). Epidemiological study of health hazards among workers handling engineered nanomaterials. *Journal of Nanoparticle Research, 14*(8), 15.

Liu, G. Z., Zhao, G. L., Meng, F. X., et al. (2012). Catalytic Cracking of Supercritical n-Dodecane over Wall-Coated HZSM-5 Zeolites with Micro- and Nanocrystal Sizes. *Energy & Fuels, 26*(2), 1220-1229.

Liu, Y. S., Walter, T. M., Chang, W. J., et al. (2007). Electrical detection of germination of viable model Bacillus anthracis spores in microfluidic biochips. *Lab on a Chip, 7*(5), 603-610.

Mao, Y. B., & Wong, S. S. (2006). Size- and shape-dependent transformation of nanosized titanate into analogous anatase titania nanostructures. *Journal of the American Chemical Society, 128*(25), 8217-8226.

Marchand, G., Delattre, C., Campagnolo, R., et al. (2005). Electrical detection of DNA hybridization based on enzymatic accumulation confined in nanodroplets. *Analytical Chemistry, 77*(16), 5189-5195.

McFarland, A. R., Haglund, J. S., King, M. D., et al. (2010). Wetted Wall Cyclones for Bioaerosol Sampling. *Aerosol Science and Technology, 44*(4), 241-252.

Meng, F., King, M. D., Hassan, Y. A., et al. (2014). Localized fluorescent complexation enables rapid monitoring of airborne nanoparticles. *Environmental Science-Nano, 1*(4), 358-366.

Morawska, L., Wang, H., Ristovski, Z., et al. (2009). JEM Spotlight: Environmental monitoring of airborne nanoparticles. *Journal of Environmental Monitoring, 11*(10), 1758-1773.

Mueller, R., Kammler, H. K., Wegner, K., et al. (2003). OH surface density of SiO2 and TiO2 by thermogravimetric analysis. *Langmuir, 19*(1), 160-165.

Nazarenko, Yevgen, Lioy, Paul, & Mainelis, Gedi. (2014). Quantitative Assessment of Inhalation Exposure and Deposited Dose of Aerosol from Nanotechnology-Based Consumer Sprays. *Environmental Science: Nano*.

Nelson, K. E., Foley, J. O., & Yager, P. (2007). Concentration gradient immunoassay. 1. An immunoassay based on interdiffusion and surface binding in a microchannel. *Analytical Chemistry, 79*(10), 3542-3548.

O'Shaughnessy, Patrick T. (2013). Occupational health risk to nanoparticulate exposure. *Environmental Science: Processes & Impacts, 15*(1), 49-62.

Obrien, R. W. (1981). The electrical conductivity of a dilute suspension of charged-particles. *Journal of Colloid and Interface Science, 81*(1), 234-248.

Ohno, T., Sarukawa, K., Tokieda, K., et al. (2001). Morphology of a TiO2 photocatalyst (Degussa, P-25) consisting of anatase and rutile crystalline phases. *Journal of Catalysis, 203*(1), 82-86.

Orsini, D. A., Ma, Y. L., Sullivan, A., et al. (2003). Refinements to the particle-into-liquid sampler (PILS) for ground and airborne measurements of water soluble aerosol composition. *Atmospheric Environment, 37*(9-10), 1243-1259.

Ozturk, S., Hassan, Y. A., & Ugaz, V. M. (2010). Interfacial Complexation Explains Anomalous Diffusion in Nanofluids. *Nano Letters, 10*(2), 665-671.

Paixao, Trlc, & Bertotti, M. (2009). Fabrication of disposable voltammetric electronic tongues by using Prussian Blue films electrodeposited onto CD-R gold surfaces and recognition of milk adulteration. *Sensors and Actuators B-Chemical, 137*(1), 266-273.

Palkar, S. A., & Schure, M. R. (1997). Mechanistic study of electrical field flow fractionation .1. Nature of the internal field. *Analytical Chemistry, 69*(16), 3223-3229.

Pamme, Nicole. (2007). Continuous flow separations in microfluidic devices. *Lab on a Chip, 7*(12), 1644-1659.

Patolsky, F., Zheng, G. F., Hayden, O., et al. (2004). Electrical detection of single viruses. *Proceedings of the National Academy of Sciences of the United States of America, 101*(39), 14017-14022.

Perry, J. M., Zhou, K. M., Harms, Z. D., et al. (2010). Ion transport in nanofluidic funnels. *Acs Nano, 4*(7), 3897-3902.

Pileni, M. P. (2003). The role of soft colloidal templates in controlling the size and shape of inorganic nanocrystals. *Nature Materials, 2*(3), 145-150.

Pumera, M. (2011). Nanomaterials meet microfluidics. *Chemical Communications, 47*(20), 5671-5680.

Rahman, M. T., Krishnamurthy, P. G., Parthiban, P., et al. (2013). Dynamically tunable nanoparticle engineering enabled by short contact-time microfluidic synthesis with a reactive gas. *Rsc Advances*, *3*(9), 2897-2900.

Ranade, M. R., Navrotsky, A., Zhang, H. Z., et al. (2002). Energetics of nanocrystalline TiO2. *Proceedings of the National Academy of Sciences of the United States of America*, *99*, 6476-6481.

Richman, E. K., & Hutchison, J. E. (2009). The nanomaterial characterization bottleneck. *Acs Nano*, *3*(9), 2441-2446.

Roa, R., Carrique, F., & Ruiz-Reina, E. (2011). dc electrokinetics for spherical particles in salt-free concentrated suspensions including ion size effects. *Physical Chemistry Chemical Physics*, *13*(43), 19437-19448.

Sadik, O. A., Zhou, A. L., Kikandi, S., et al. (2009). Sensors as tools for quantitation, nanotoxicity and nanomonitoring assessment of engineered nanomaterials. *Journal of Environmental Monitoring*, *11*(10), 1782-1800.

Sarojini, K. G. Kalpana, Manoj, Siva V., Singh, Pawan K., et al. (2013). Electrical conductivity of ceramic and metallic nanofluids. *Colloids and Surfaces a-Physicochemical and Engineering Aspects*, *417*, 39-46.

Satoh, N., Nakashima, T., Kamikura, K., et al. (2008). Quantum size effect in TiO2 nanoparticles prepared by finely controlled metal assembly on dendrimer templates. *Nature Nanotechnology*, *3*(2), 106-111.

Scanlon, D. O., Dunnill, C. W., Buckeridge, J., et al. (2013). Band alignment of rutile and anatase TiO2. *Nature Materials*, *12*(9), 798-801.

Schoch, R. B., Han, J. Y., & Renaud, P. (2008). Transport phenomena in nanofluidics. *Reviews of Modern Physics, 80*(3), 839-883.

Shklover, V., Nazeeruddin, M. K., Zakeeruddin, S. M., et al. (1997). Structure of nanocrystalline TiO2 powders and precursor to their highly efficient photosensitizer. *Chemistry of Materials, 9*(2), 430-439.

Sigmund, W. M., Bell, N. S., & Bergstrom, L. (2000). Novel powder-processing methods for advanced ceramics. *Journal of the American Ceramic Society, 83*(7), 1557-1574.

Song, Y. J., Hormes, J., & Kumar, Cssr. (2008). Microfluidic synthesis of nanomaterials. *Small, 4*(6), 698-711.

Sotiriou, Georgios A., Watson, Christa, Murdaugh, Kimberly M., et al. (2014). Engineering safer-by-design silica-coated ZnO nanorods with reduced DNA damage potential. *Environmental Science: Nano, 1*(2), 144-153.

Sun, T., Bernabini, C., & Morgan, H. (2009). Single-colloidal particle impedance spectroscopy: complete equivalent circuit analysis of polyelectrolyte microcapsules. *Langmuir, 26*(6), 3821-3828.

Takagi, J., Yamada, M., Yasuda, M., et al. (2005). Continuous particle separation in a microchannel having asymmetrically arranged multiple branches. *Lab on a Chip, 5*(7), 778-784.

Tang, C. K., Vaze, A., & Rusling, J. F. (2012). Fabrication of immunosensor microwell arrays from gold compact discs for detection of cancer biomarker proteins. *Lab on a Chip, 12*(2), 281-286.

Testino, A., Bellobono, I. R., Buscaglia, V., et al. (2007). Optimizing the photocatalytic properties of hydrothermal TiO2 by the control of phase composition and particle morphology. A systematic approach. *Journal of the American Chemical Society, 129*(12), 3564-3575.

Tritscher, T., Beeston, M., Zerrath, A. F., et al. (2013). NanoScan SMPS - A Novel, Portable Nanoparticle Sizing and Counting Instrument. *Nanosafe 2012: International Conferences on Safe Production and Use of Nanomaterials, 429*, 10.

Trouiller, B., Reliene, R., Westbrook, A., et al. (2009). Titanium Dioxide Nanoparticles Induce DNA Damage and Genetic Instability In vivo in Mice. *Cancer Research, 69*(22), 8784-8789.

Tsai, C. J., Liu, C. N., Hung, S. M., et al. (2012). Novel Active Personal Nanoparticle Sampler for the Exposure Assessment of Nanoparticles in Workplaces. *Environmental Science & Technology, 46*(8), 4546-4552.

US National Academy of Sciences. (2012). A Research Strategy for Environmental, Health, and Safety Aspects of Engineered Nanomaterials.

US National Institue for Occupational Safety and Health (NIOSH). (2011). Current Intelligence Bulletin 63: Occupational Exposure to Titanium Dioxide.

Vahey, M. D., & Voldman, J. (2009). High-throughput cell and particle characterization using isodielectric separation. *Analytical Chemistry, 81*(7), 2446-2455.

Vejerano, Eric P., Leon, Elena C., Holder, Amara L., et al. (2014). Characterization of particle emissions and fate of nanomaterials during incineration. *Environmental Science: Nano*.

Wang, H. Z., Li, X. Y., Uehara, M., et al. (2004). Continuous synthesis of CdSe-ZnS composite nanoparticles in a microfluidic reactor. *Chemical Communications*(1), 48-49.

Wang, H. Z., Nakamura, H., Uehara, M., et al. (2002). Preparation of titania particles utilizing the insoluble phase interface in a microchannel reactor. *Chemical Communications*(14), 1462-1463.

Wang, J. J., Sanderson, B. J. S., & Wang, H. (2007). Cyto- and genotoxicity of ultrafine TiO2 particles in cultured human lymphoblastoid cells. *Mutation Research-Genetic Toxicology and Environmental Mutagenesis, 628*(2), 99-106.

Weir, A., Westerhoff, P., Fabricius, L., et al. (2012). Titanium Dioxide Nanoparticles in Food and Personal Care Products. *Environmental Science & Technology, 46*(4), 2242-2250.

Williams, B. J., Goldstein, A. H., Kreisberg, N. M., et al. (2006). An in-situ instrument for speciated organic composition of atmospheric aerosols: Thermal Desorption Aerosol GC/MS-FID (TAG). *Aerosol Science and Technology, 40*(8), 627-638.

Win-Shwe, T. T., & Fujimaki, H. (2011). Nanoparticles and Neurotoxicity. *International Journal of Molecular Sciences, 12*(9), 6267-6280.

Yu, H. Z., Li, Y. C., & Ou, L. M. L. (2012). Reading Disc-Based Bioassays with Standard Computer Drives. *Accounts of Chemical Research, 46*(2), 258-268.

Zhang, J. H., Thurber, A., Tenne, D. A., et al. (2010). Enhanced Dye Fluorescence in Novel Dye-ZnO Nanocomposites. *Advanced Functional Materials, 20*(24), 4358-4363.

Zhou, Yue, Irshad, Hammad, Tsai, Chuen-Jinn, et al. (2013). Evaluation of a novel personal nanoparticle sampler. *Environmental Science: Processes & Impacts, 16*(2), 203-210.

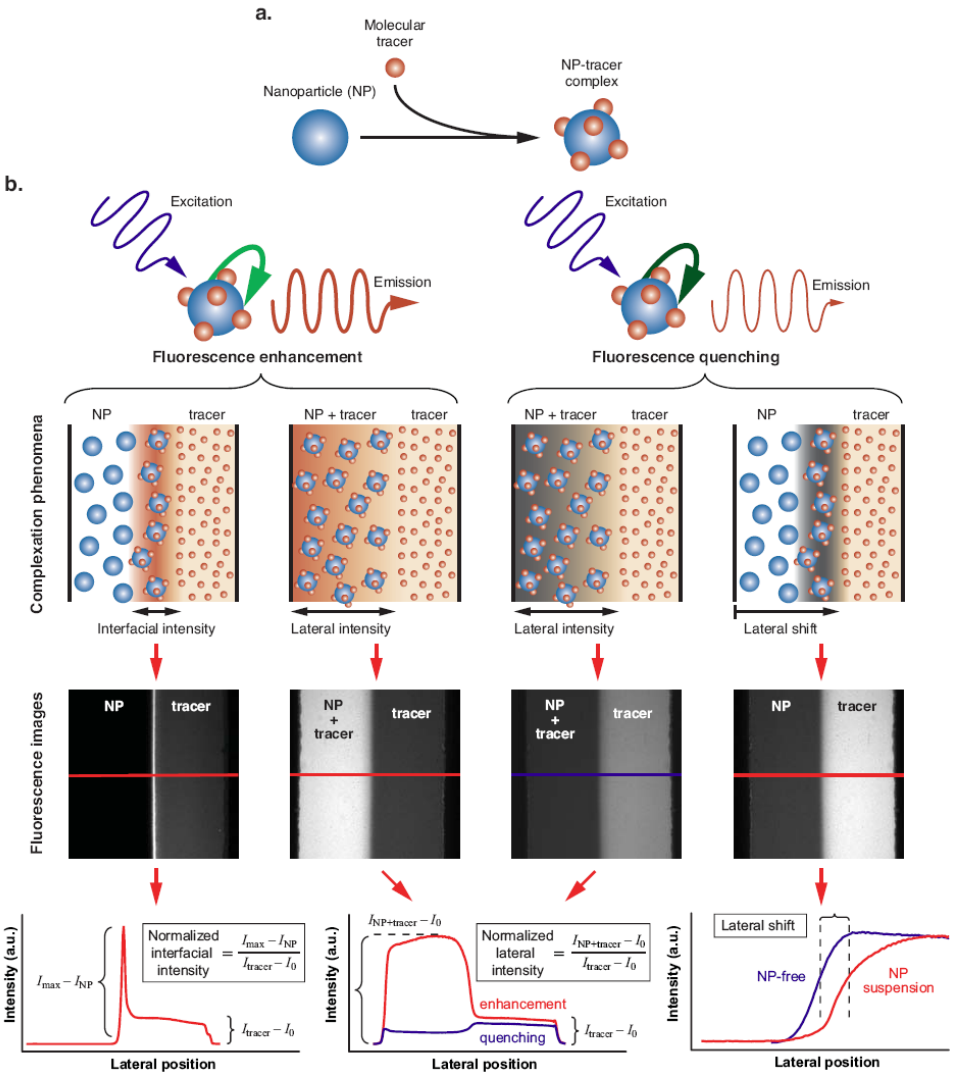

Figure 1. Analysis and quantification of fluorescent complexation.
(a) Distinct fluorescence signatures emerge from surface complexation between nanoparticles and a molecular tracer. (b) These phenomena can be continuously observed by establishing a sharp (micron scale) gradient between adjacent nanoparticle and tracer streams in a microscale laminar flow environment (flow direction is vertical). Nanoparticle size and concentration information is embedded in the interfacial and lateral features of the corresponding fluorescence images. The intensity profiles can be quantified in multiple ways depending on the strength of the fluorescence signal and whether enhancement or quenching are observed. Illustrative diagrams are qualitative and not drawn to scale.

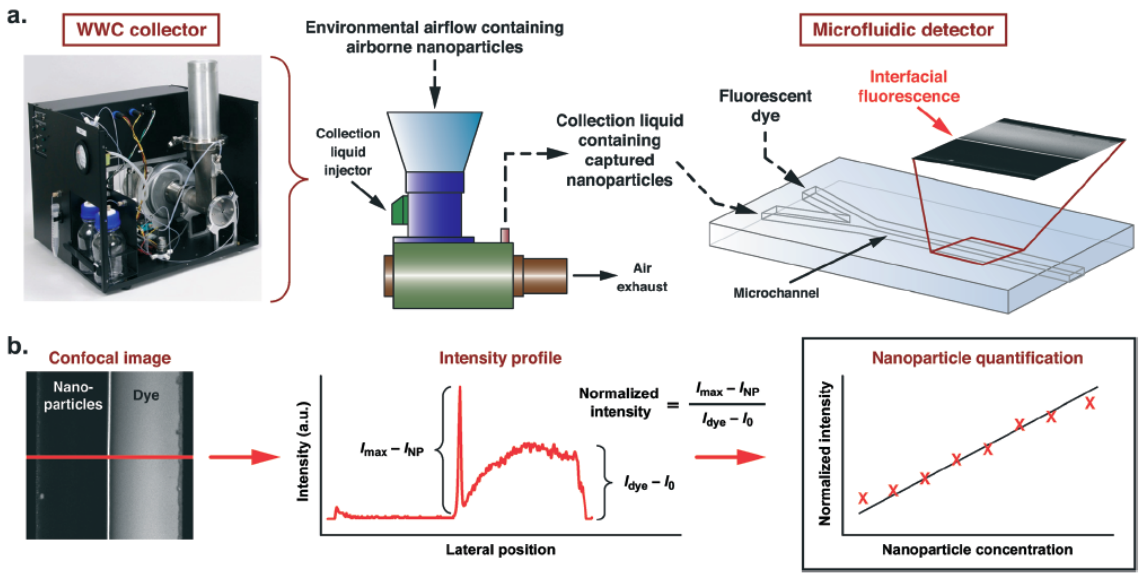

Figure 2. Integrated high-throughput monitoring.
(a) Airborne environmental nanoparticles are collected and concentrated by a WWC, then co-injected into a microchannel in parallel with a tracer dye. A pronounced material-dependent interfacial fluorescence signature emerges due to local dye-nanoparticle complexation between co-flowing streams in the microchannel. (b) The peak value in the lateral intensity profile is scaled with respect to baseline values in the nanoparticle and dye streams (INP and I0, respectively), yielding a normalized self-calibrated quantity that can be directly correlated with nanoparticle concentration (Meng, King, Hassan, & Ugaz, 2014). (Reproduced by permission of the Royal Society of Chemistry)

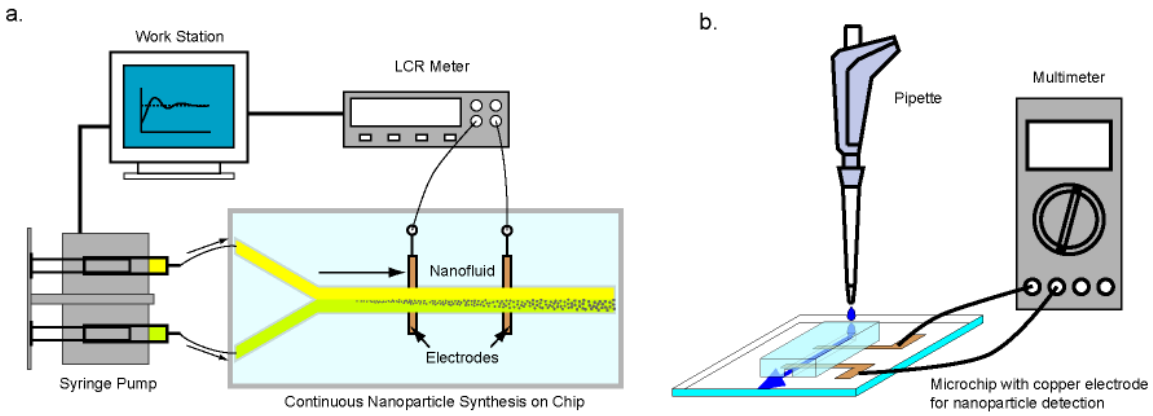

Figure 3. Two modes are utilized to characterize nanoparticles by electrical conductivity.
(a) Scheme of continuous synthesis and quality control. A nanoparticle suspension's resistance is detected and analyzed. The corresponding output is used to adjust the feed pump flow rate, increasing or decreasing the residence time inside microchannel to control properties of the synthesized particles. (b) Offline nanoparticle characterization can also be performed on nanoliter samples using a low-cost multimeter

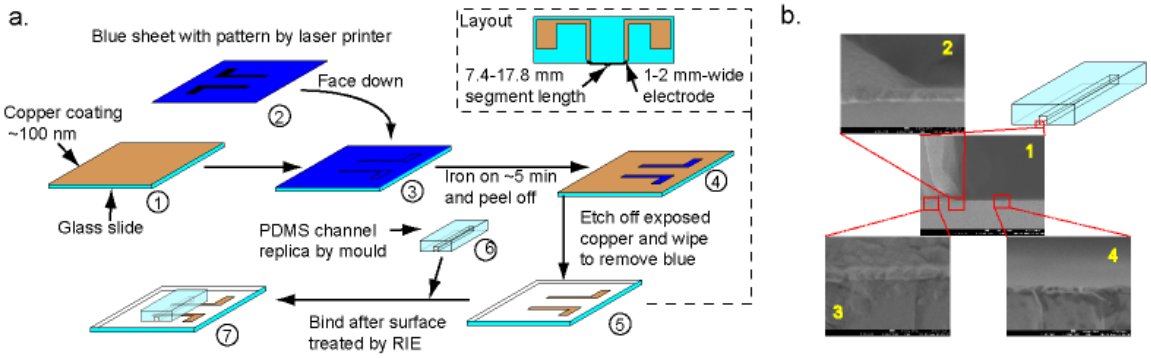

Figure 4. Electrodes fabrication and characterization.

(a) Simply process to fabricate electrode pattern insert microchannel. (1) Glass slide is coated a thin copper layer (~100 nm) by metal sputter; (2) A black pattern is printed on blue sheet by commercial black and white laser printer; (3) Face down blue sheet to contact printed black pattern with copper layer on glass; (4) Use iron to press and heat blue sheet for about 5 minutes to transfer pattern on to the copper layer, and peel off the blue sheet, leaving blue pattern on copper layer; (5) Etch the copper layer in gold etcher to remove the uncovered copper, obtaining blue pattern on glass. Then carefully wipe blue cover off with acetone and rinse by DI water, achieving copper pattern on glass; (6) Use mould, which has been prepared by lithograph as previous description, to replicate a PDMS channel and (7) Use RIE to treat PDMS channel surface and glass surface with copper pattern. Then bind treated surfaces to form a enclosed channel with a copper electrode insert to measure EC inside microfluidics. (b) SEM images for (1) channel cross section; (2) PDMS wall-copper-glass binding part; (3) PDMS-copper-glass binding part and (4) copper-glass binding part.

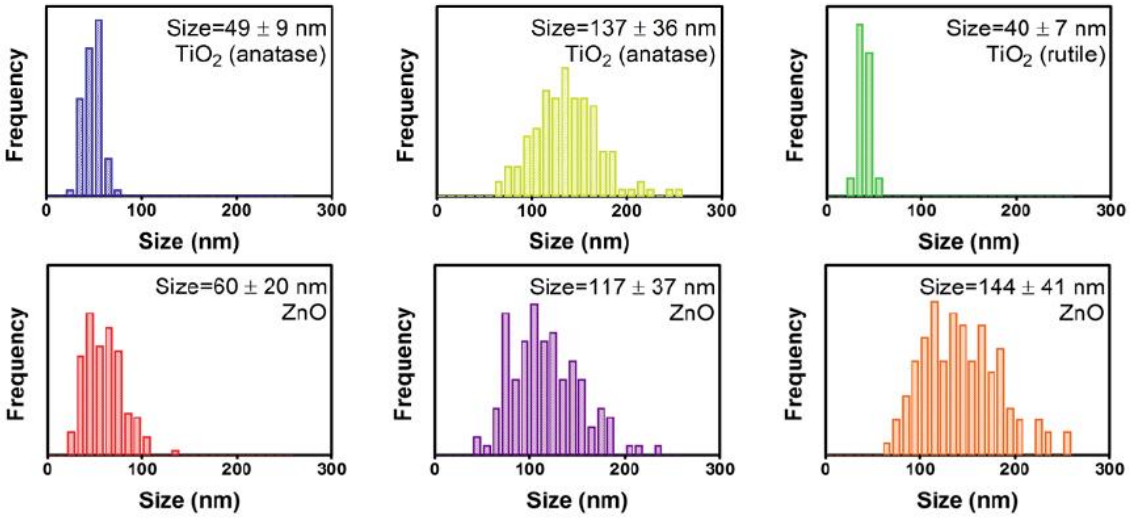

Figure 5. Size distribution data obtained from SEM analysis of nanomaterials studied in the main text.

(a) TiO_2 (anatase), 49 ± 9 nm and (b) 137 ± 36 nm, (c) TiO_2 (rutile), 40 ± 7 nm, ZnO (d) 60 ± 20 nm, (e) 117 ± 37 nm and (f) 144 ± 41 nm.

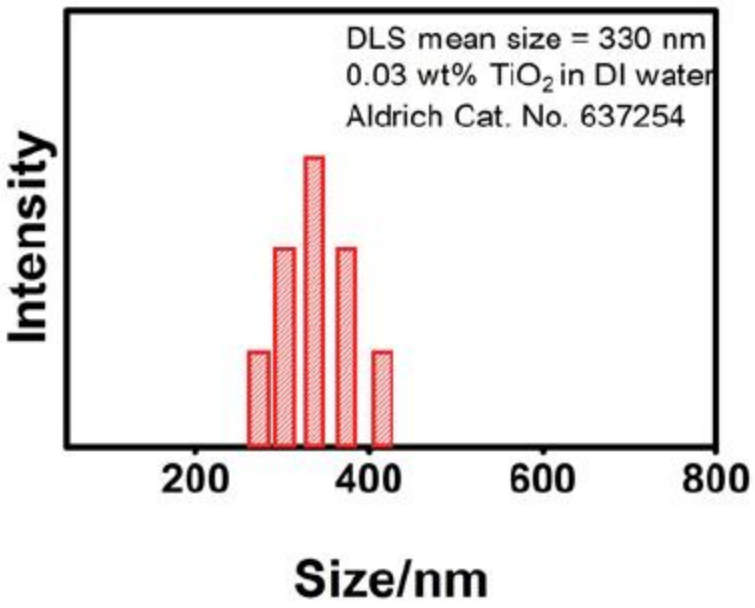

Figure 6. DLS analysis of anatase TiO_2 nanoparticles. The mean particle size of 49 ± 9 nm obtained via SEM is overestimated by DLS.

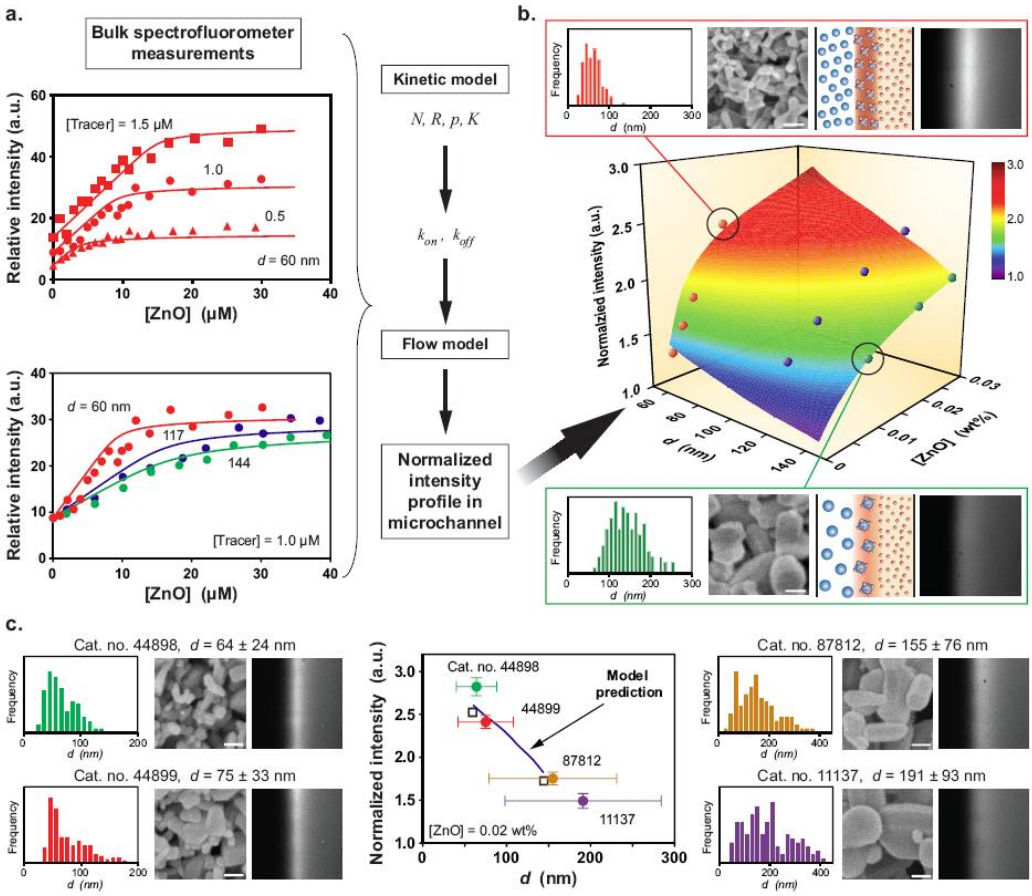

Figure 7. ZnO nanoparticle size and concentration information are embedded in the interfacial fluorescence signature.
(a) Bulk spectrofluorometer measurements at different tracer concentrations are first performed using 60 ± 20 nm particles followed by subsequent measurements as a function of particle size using 117 ± 37 and 144 ± 41 nm nanoparticles to obtain kinetic parameters. (b) These parameters serve as inputs to a flow model that captures the combined effect of particle size and concentration on the fluorescence signature (normalized interfacial intensity) measured in a microchannel experiment ([Tracer] = 5 μM). Insets show SEM images and corresponding size distributions of nanoparticle powders (bars, 100 nm) along with the observed fluorescence profile (microchannels are 500 μm wide). (c) The surface plot in (b) enables instantaneous sizing of 4 different aqueous ZnO suspensions prepared from commercial nanopowders based on interfacial intensity measurements. Vertical error bars represent the standard deviation of 3 independent microchannel-based fluorescence measurements, horizontal error bars represent the standard deviation of corresponding SEM particle size (n > 100). Open squares show model predictions that represent polydispersity effects by considering the full ensemble of coupled multiple dye-nanoparticle interactions across the entire size distribution for the 60 and 144 nm materials in (a)

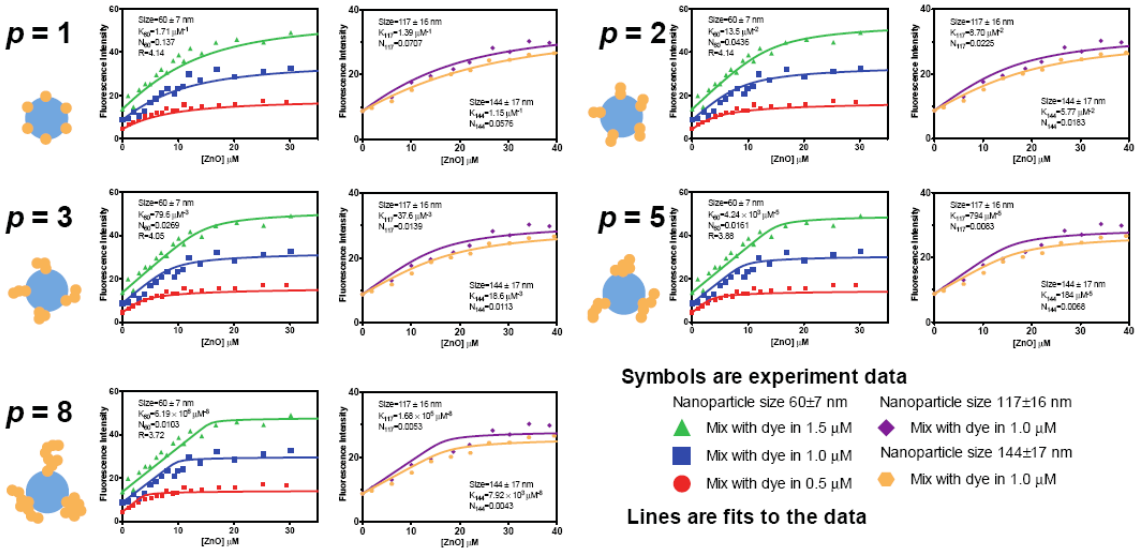

Figure 8. Determination of kinetic parameters from spectrofluorometer data. Aqueous suspensions of ZnO nanoparticles (60 ± 20 nm) with initial concentration ranging from 1 to 30 μM were mixed with a fluorescein tracer at concentrations of 0.5, 1.0 and 1.5 μM respectively and analyzed by steady emission scan in a spectrofluorometer. Values of K, N and R yielding best fits to the data were determined at discrete increments of the parameter p. The analysis was repeated to determine parameters corresponding to nanoparticles of different size (117 ± 16 and 144 ± 17 nm).

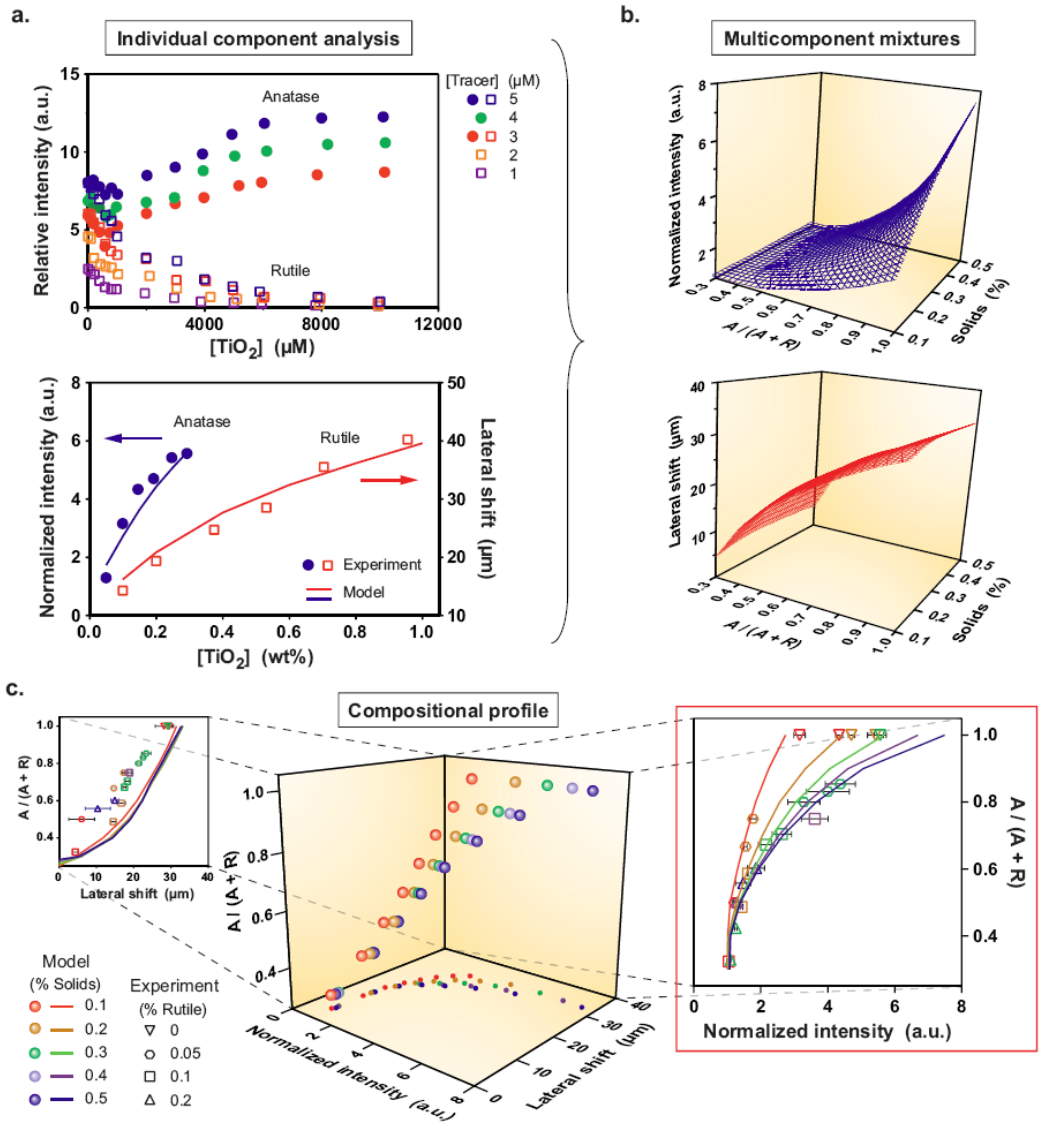

Figure 9. Quantitative composition analysis of anatase and rutile TiO_2 nanoparticle mixtures.

(a) Kinetic parameters are obtained from the bulk fluorescence response displayed by each nanoparticle species (anatase: enhancement, 49 ± 9 nm, rutile: quenching, 40 ± 7 nm), enabling the corresponding fluorescence (normalized interfacial intensity, lateral shift) measured in microchannel experiments to be predicted. (b) The flow model is then used to map these fluorescence signatures for anatase and rutile mixtures over an ensemble of compositions (expressed in terms of the anatase mass fraction, anatase / (anatase + rutile) = A / (A + R), [Tracer] = 5 μM) . (c) These data are then cross-plotted so that the anatase fraction can be uniquely determined from simultaneous normalized interfacial intensity and lateral shift measurements over a range of compositional states.

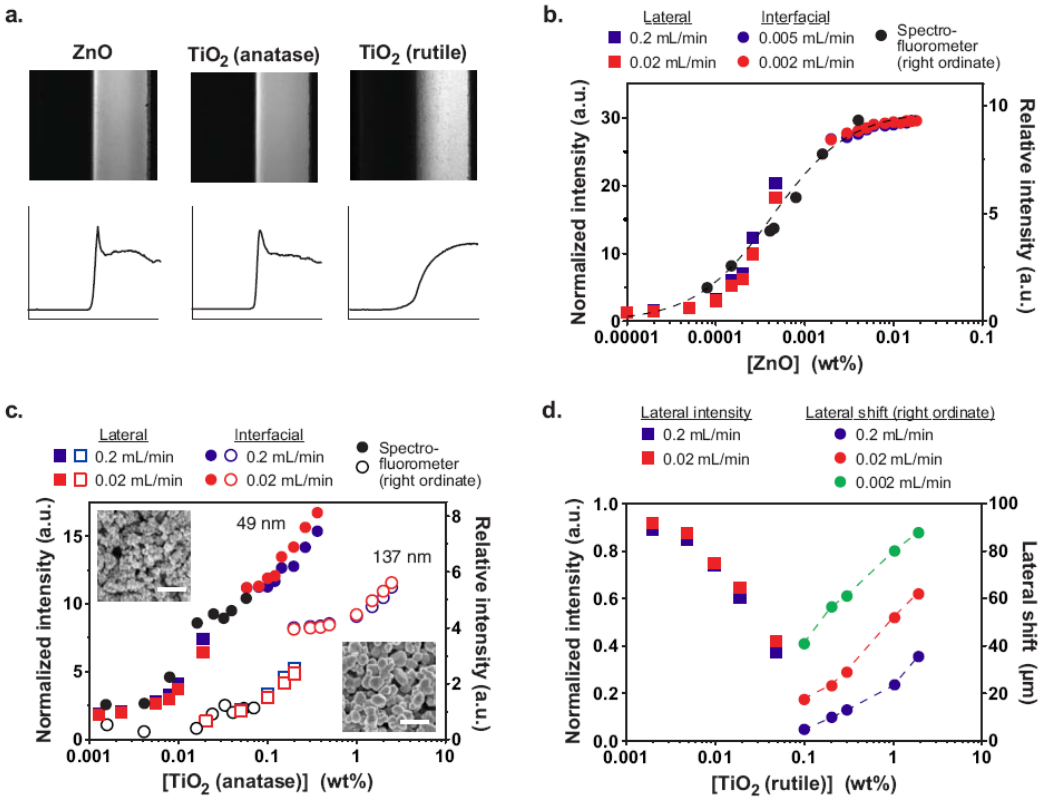

Figure 10. Fluorescent complexation sensitively depends on nanoparticle concentration, species, size, and morphology.
(a) The material-dependence of interfacial fluorescence becomes evident upon comparison of ZnO (60 ±20 nm) and TiO_2 (anatase: 49 ±9 nm; rutile: 137 ±36 nm). Image left half: 50 mM nanoparticle suspension; image right half: 0.033 mg mL^{-1} fluorescein tracer. Upper panels show images of co-flowing streams, lower show the corresponding lateral intensity profile (microchannels are 500 μm wide). (b) Broad quantitative sensitivity over 4 orders of magnitude of nanoparticle concentration is attained by combining data from interfacial and pre-mix approaches (dashed line connecting the spectrofluorometer data points is included to guide the eye, a constant vertical shift factor was applied to align the lateral and interfacial data to clearly depict the concentration dependent trend). (c) Fluorescent complexation is sensitively dependent on nanoparticle size, enabling differences to be distinguished independent of agglomeration state (insets show SEM images of nanoparticle powders, bar 400 nm). (d) Morphological sensitivity is evident by transformation from fluorescence enhancement in anatase TiO_2 to quenching in rutile TiO_2, where characterization in terms of the interfacial shift distance enables the accessible concentration range to be greatly extended (dashed lines connecting the shift distance data are included to guide eye). Particle sizes were obtained by analysis of SEM data, [Tracer] = 0.0165 mg mL^{-1} in (b), (c), and (d).

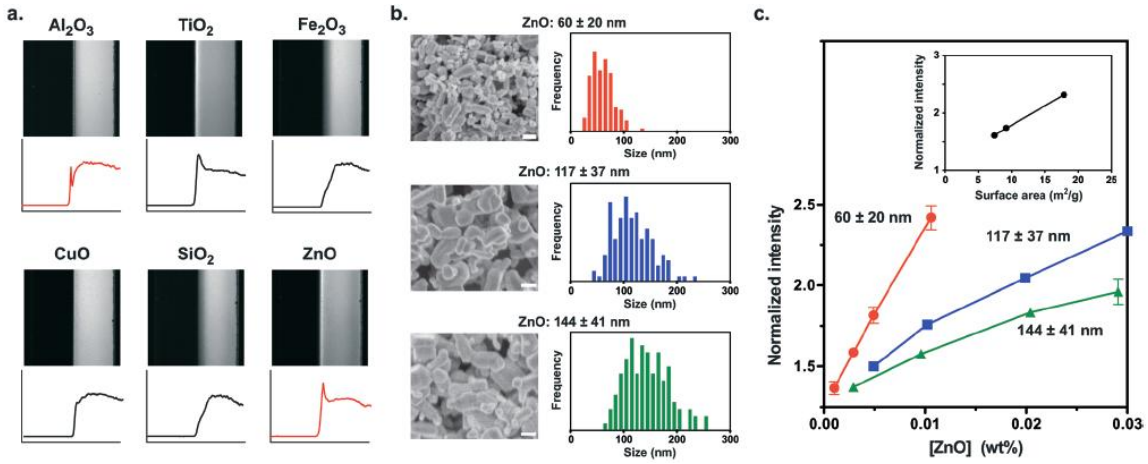

Figure 11. Composition and size dependence of fluorescent complexation.
(a) The material-dependent nature of dye-nanoparticle complexation is evident by characteristic features in the observed lateral fluorescence intensity profiles (left half of the images: 50 mM nanoparticle suspension stabilized with 5 mg mL^{-1} Tween 20; right half of the images: 0.033 mg mL^{-1} fluorescein solution; flow rate, 0.2 mL min^{-1}). Upper panels show images of co-flowing streams, lower panels show the corresponding lateral intensity profile (see Figure. 1b; microchannels are 500 μm wide). (b, c) The size dependence of interfacial complexation is illustrated using ZnO nanoparticles. (b) Size distribution data obtained from ensembles of at least 100 particles in the SEM images (scale bar in SEM, 100 nm). (c) Enhancement in fluorescence intensity is maximized at small particle sizes where the surface area to volume ratio is greatest (0.00165 mg mL^{-1} fluorescein solution; flow rate, 0.005 mL min^{-1}; error bars, mean ± sd of at least 3 independent experiments). Inset: fluorescence intensity is proportional to particle surface area for a given mass of nanoparticles. Surface areas are determined using the particle diameter data in (b) and a spherical particle density of 5.6 g cm^{-3} (solid line, linear regression fit) (Meng et al., 2014). (Reproduced by permission of the Royal Society of Chemistry)

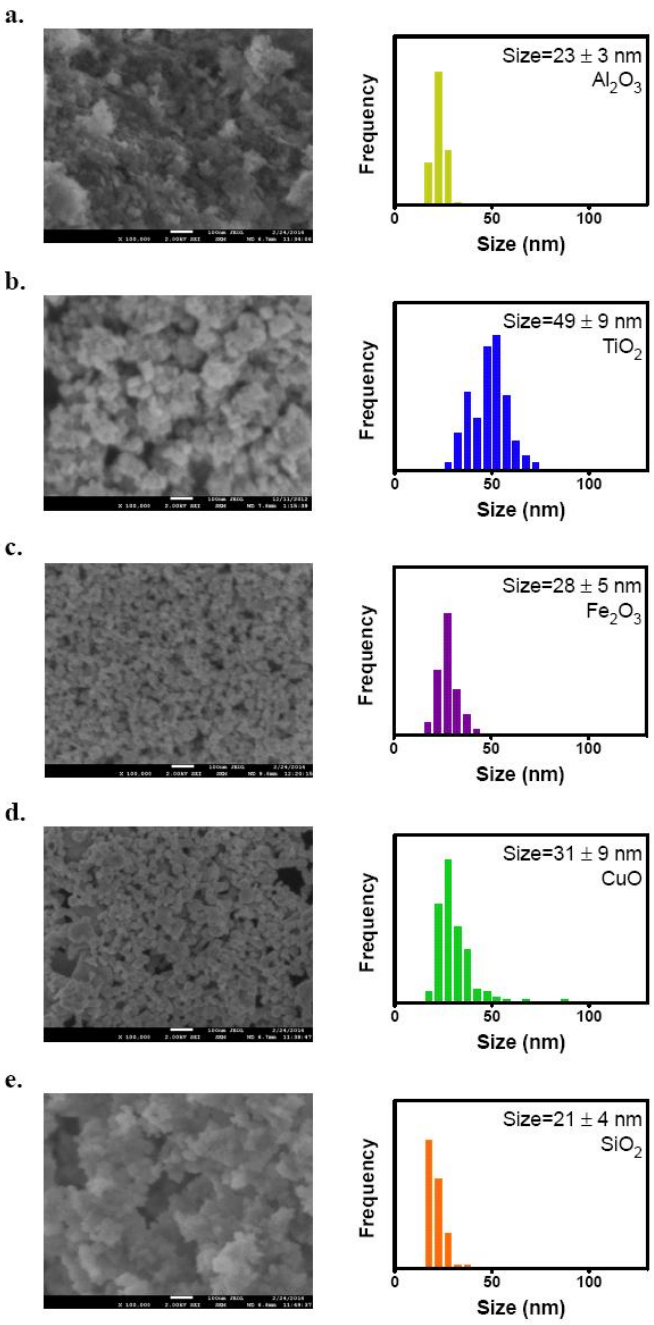

Figure 12. SEM images (left) and size distribution data (right) of (a) Al_2O_3, (b) TiO_2, (c) Fe_2O_3, (d) CuO, and (e) SiO_2 nanomaterial powders reported in Figure 11a of the main text.

Particle sizes obtained from the SEM images are in agreement with the manufacturer-specified values (Meng et al., 2014). (Reproduced by permission of the Royal Society of Chemistry)

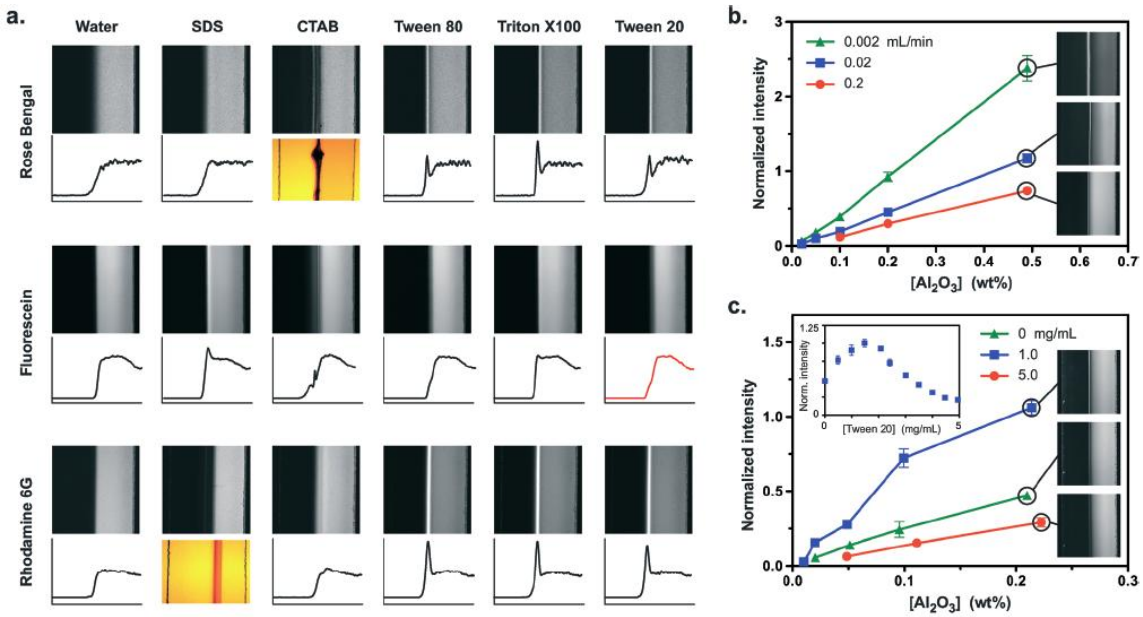

Figure 13. The microfluidic detection component operates efficiently under conditions compatible with continuous nanoparticle collection.
(a) Interactions between candidate fluorescent dyes (right half of the image) and stabilizing surfactants (left half of the image) were first assessed. The combination of fluorescein and Tween 20 (the surfactant typically added to the WWC collection liquid) minimally altered interfacial fluorescence, motivating us to select this formulation for subsequent experiments. Photos are shown in cases where severe complexation distorted the lateral intensity profile. Dye concentrations: 0.5 mg mL^{-1} (Rose Bengal), 0.033 mg mL−1 (fluorescein), and 0.048 mg mL^{-1} (Rhodamine 6G). All experiments were performed at 0.02 mL min^{-1} using surfactant concentrations of 5 mg mL−1. Upper panels show images of co-flowing streams; lower panels show the corresponding lateral intensity profile (see Figure. 1b; microchannels are 500 μm wide). (b–c) Characterization experiments using standard test suspensions containing ultrafine Al_2O_3 nanoparticles co-injected with a 0.033 mg mL^{-1} fluorescein solution. (b) Pronounced interfacial fluorescence is observed over a range of flow rates compatible with the WWC fluidic output (3 mg mL^{-1} Tween 20). (c) A peak in interfacial fluorescence is observed at intermediate surfactant concentrations (main plot, [Al_2O_3] dependence at 3 different [Tween 20]; inset, [Tween 20] dependence at [Al_2O_3] = 0.2 wt%; flow rate in both, 0.02 mL min^{-1}). Pronounced fluorescence is observed at the standard 0.1 mg mL^{-1} Tween 20 loading in the WWC collection liquid. Error bars in (b) and (c), mean ± sd of at least 3 independent experiments (Meng et al., 2014). (Reproduced by permission of the Royal Society of Chemistry)

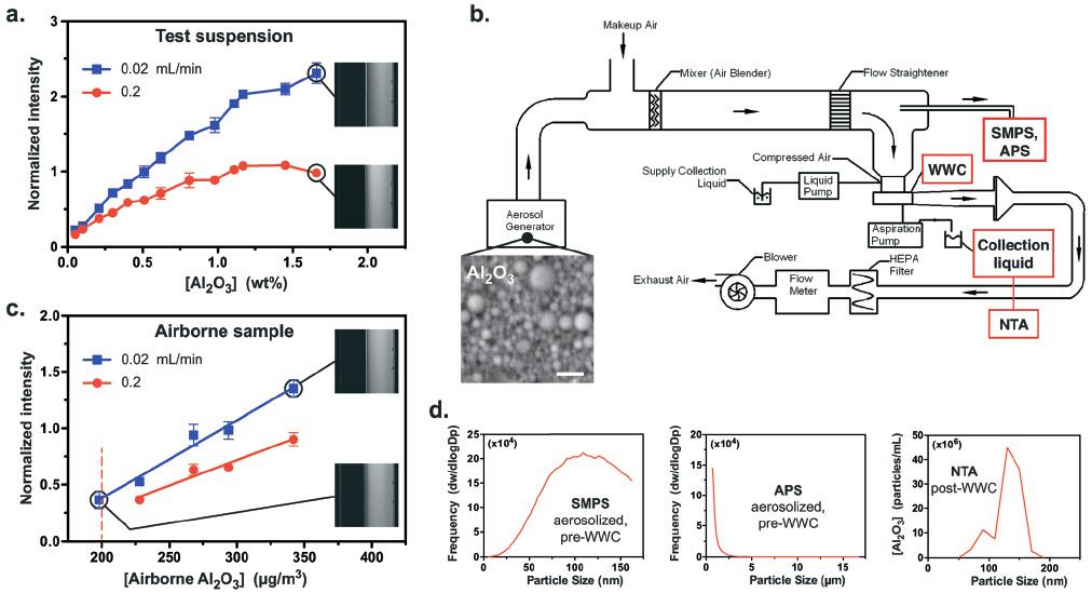

Figure 14. High-throughput collection and detection of airborne nanoparticles. (a) The concentration dependence of interfacial fluorescence was first established using a standard Al_2O_3 test suspension co-injected with a 0.033 mg mL^{-1} fluorescein solution matching WWC operation condition. (b) Overview of the flow cell and test chamber to evaluate environmental sampling of aerosolized airborne nanoparticles. The concentration of airborne ultrafine nanoparticles inside the chamber (prior to WWC collection) was quantified using SMPS (scale bar in SEM, 200 nm). (c) A correlation was then established between the airborne environmental nanoparticle concentration in the test chamber and interfacial fluorescence in the microchannel (solid lines show linear regression fits), indicating a detection limit below 200 μg m^{-3} (dashed line). The collection liquid containing sampled nanoparticles and 0.1 mg mL^{-1} Tween 20 was co-injected with 0.033 mg mL^{-1} fluorescein. (d) Multiscale size distribution analysis of the aerosolized Al_2O_3 nanoparticles before and after WWC collection. Dry nanoparticles dispersed in the chamber using a Collison atomizer were characterized prior to WWC collection using SMPS (top, 4–150 nm ultrafine size range) and aerodynamic particle sizing (APS, middle, 0.5–20 μm range). Nanoparticles dispersed in the collection liquid after passing through the WWC were also directly characterized using nanoparticle tracking analysis (NTA, NanoSight LM 10, bottom). The SMPS and NTA data confirm that the ultrafine size distribution is not visibly altered by either aerosolization or WWC collection, while the APS data display no evidence of agglomeration in the aerosol. The SMPS size distribution is truncated because the nano differential mobility analyzer (Nano DMA) was employed to provide optimal characterization in the ultrafine range. Error bars in (a) and (c), mean ± sd of at least 3 independent experiments (Meng et al., 2014). (Reproduced by permission of the Royal Society of Chemistry).

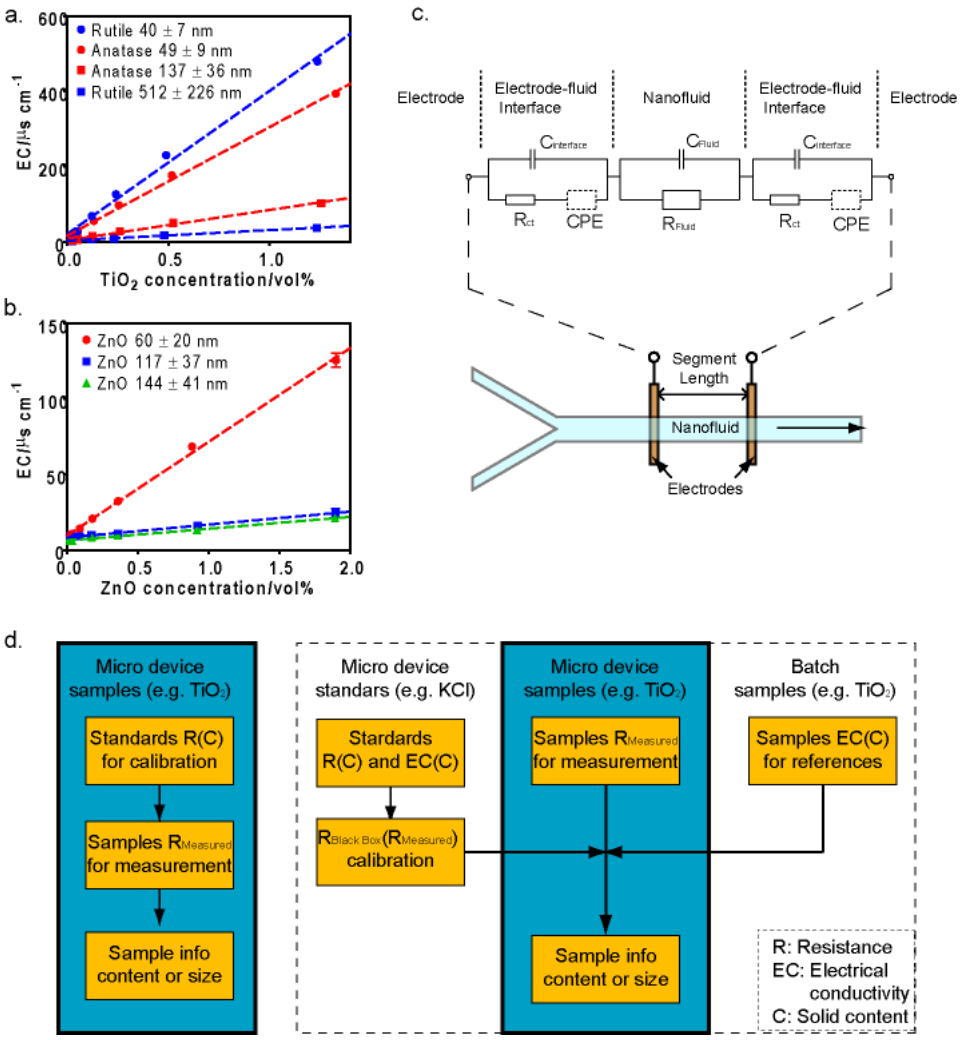

Figure 15. Bulk electrical conductivity (EC) mapping and circuit model for measurement.

The bulk electrical conductivity (EC) increases as (a) TiO_2 and (b) ZnO content increases. Linear fitting lines are show in Table 8 for each particle size series. Smaller particles result in higher EC in bulk suspension. (c) Circuit model for our approach shows theory to measure following electrical resistance inside microchannel. (d) There are two ways to apply our micro device to measure the nanoparticle suspension. The left procedure demonstrates, whenever a measurement begins, a calibration is necessarily need, which uses standards with same materials as the samples, before the samples measurement is facilitated to provide the samples' information (e.g. content, size). The right procedure displays several pre-calculated $R_{Black\ Box}$ or relations of samples' EC versus content can be stored, and when a measurement begins, these pre-stored data could be integrated with in-situ measured signal to fast show the samples' information.

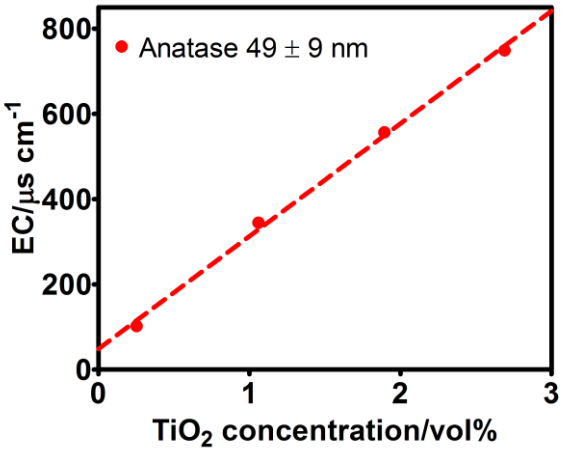

Figure 16. Fitted slope and intercept can be slight sensitive to the range of selected TiO_2 content in sample.

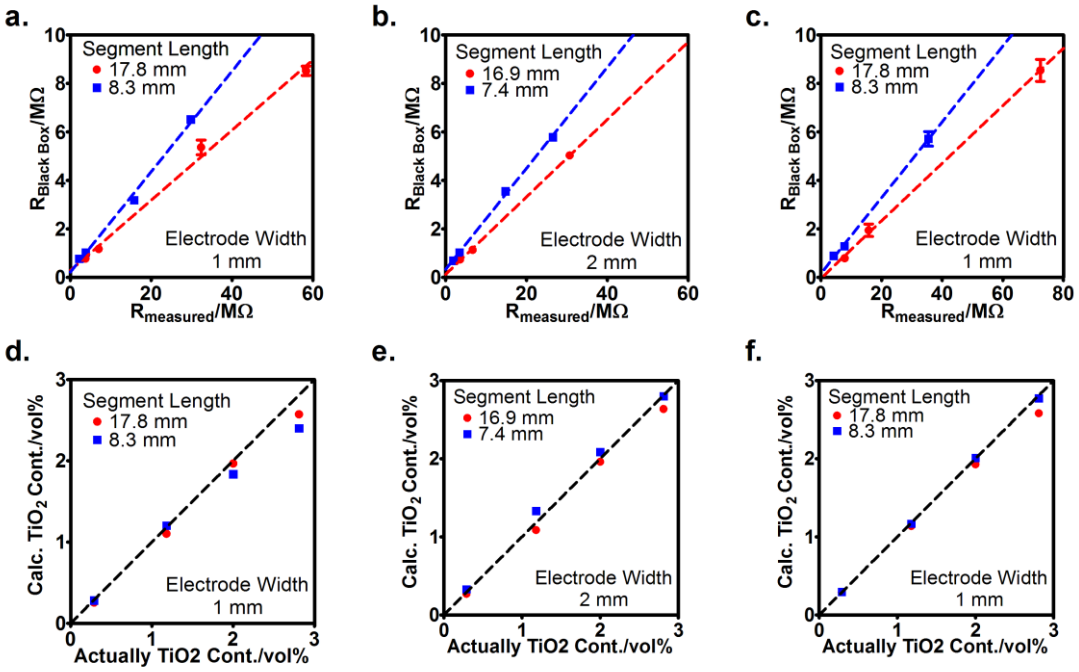

Figure 17. Electrical conductivity can be successfully measured via micro devices and give nanoparticle information.

(a-c) Upper panels shows the correlation of $R_{Black\ Box}$ to $R_{measured}$ and (d-f) lower panel shows particle contents could be eventually calculated from $R_{measured}$to compared with actually contents. y=x line is shown to better evaluate the results. (a), (b), (d) and (e) use 80 micro meter channel height, 500 micro meter width; while (c) and (f) use 40 micro height, 500 micro meter width. The measured fluid lengths and electrode widths are remarked respectively.

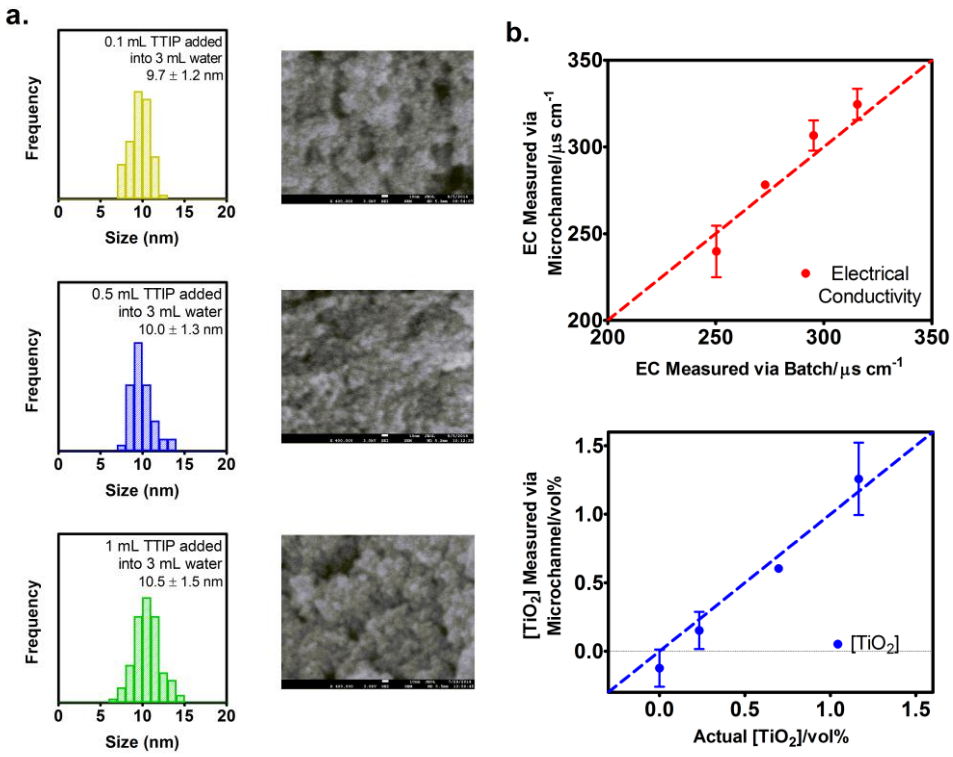

Figure 18. (a) SEM images are shown for continuous synthesized TiO_2 and their size distribution. (b) The ECs measured via microchannel match well with those measured via batch and TiO_2 contents match well with the actually prepared samples

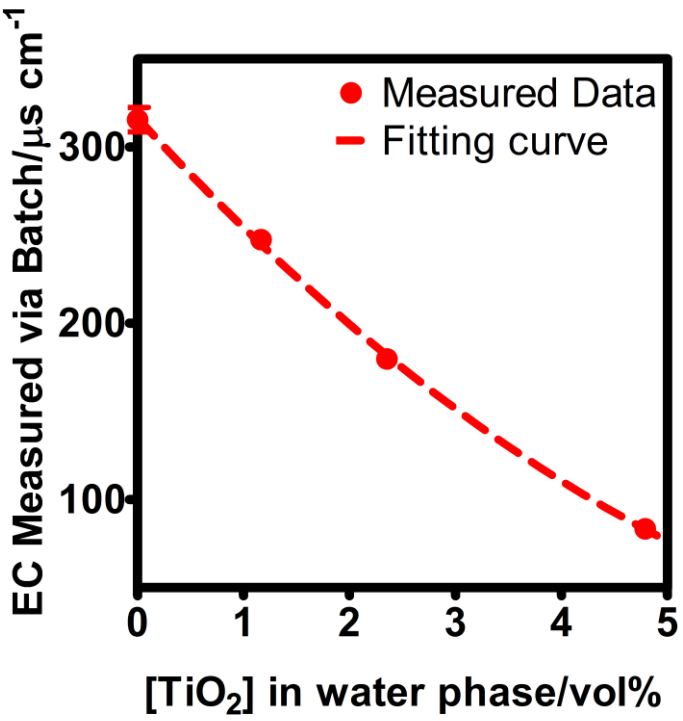

Figure 19. Fitting curve is used to determine EC or TiO_2 whenever one of them is known.

Dispersed TTIP (add IPA to 10 mL) was added into dispersed KCl water solution (3 mL 0.2 mol/L KCl aqueous solution is dispersed by IPA to 10 mL) to produce TiO_2 in batch. The suspension was stirred for 30 min and the measured EC was correlated to final TiO_2 vol% in water phase (values calculated by theoretical yield) in water phase. Fitting curve is used to determine EC or TiO_2 content whenever one of them is known.

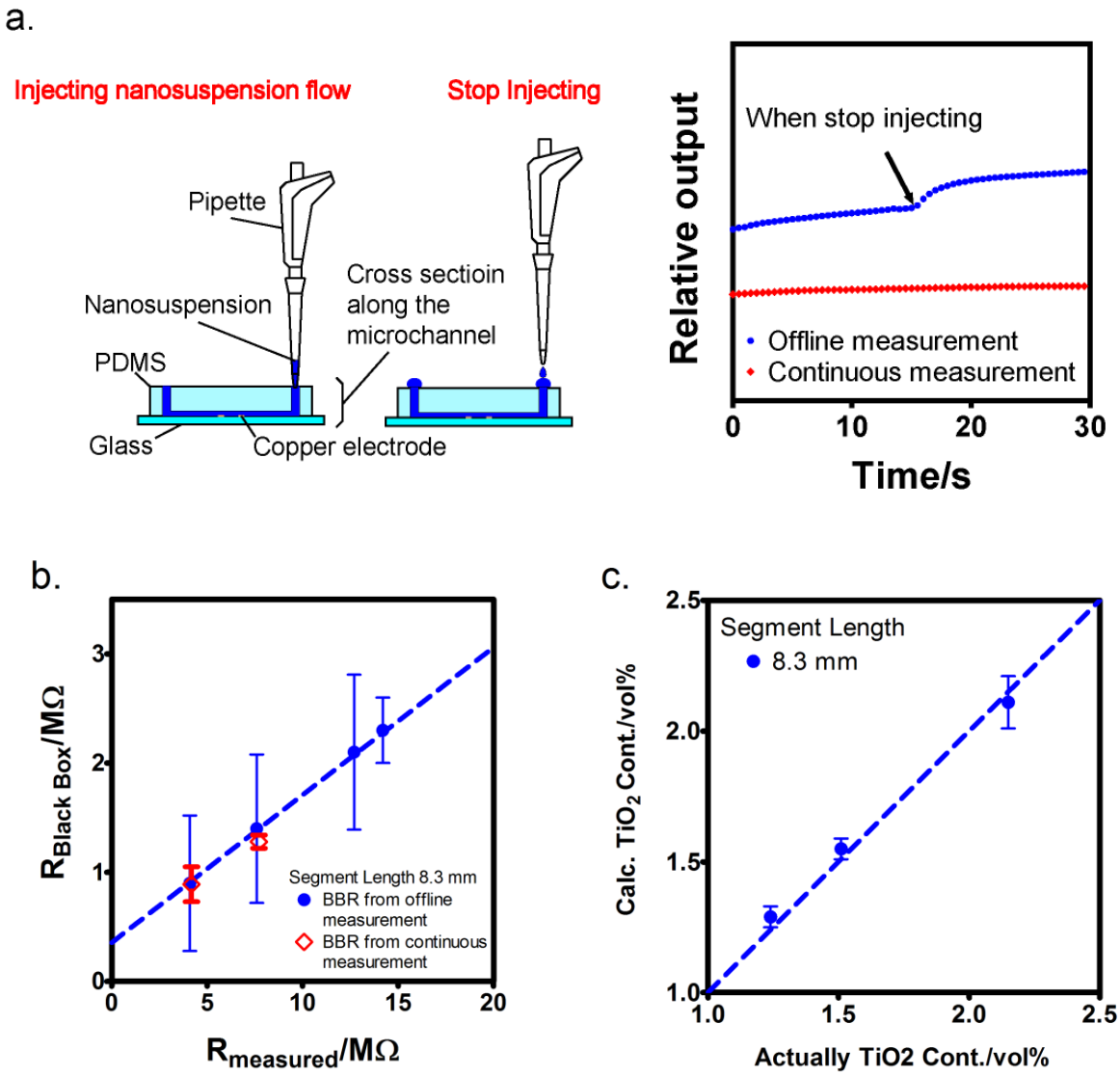

Figure 20. Black Box Resistance from offline measurement using our device and TiO_2 correlation.

(a) Offline measurement is slightly disturbed by injecting process. A typical resistance output ($R_{measured}$) versus time from multimeter for offline measurement is compared with continuous measurement by LCR meter respectively. Under offline measurement, when the injected flow is off, a jump came out and fluctuation occurred to disturb the measurement. (b) $R_{Black\ Box}$ from offline measurement using our device can be obtained with larger instability and c) TiO_2 correlation is nicely achieved by offline measurement.

Table 1. Summary of nanomaterials, dye and surfactants employed in our experiments.

Material	Composition	Vendor	Particle size measured by SEM (nm)	Density (g/cm3)
Al2O3	15 wt% suspension (aq) (Figs. 13 and 14)	NEI Corporation	~ 100	4.0
Al2O3	Powder (Fig. 11b)	Sigma-Aldrich (Cat. No. 544833)	23 ±3	4.0
Fe2O3	Powder	Sigma-Aldrich (Cat. No. 544884)	28 ±5	5.1
CuO	Powder	Alfa Aesar (Cat. No. 44928)	31 ±9	~6.4
SiO2	Powder	Sigma-Aldrich (Cat. No. 637238)	21 ±4	2.2-2.6
TiO2 (anatase)	Powder	Sigma-Aldrich (Cat. No. 637254)	49 ±9	3.9
TiO2 (anatase)	Powder	Sigma-Aldrich (Cat. No. 232033)	137 ±36	3.9
TiO2 (rutile)	Powder	Sigma-Aldrich (Cat. No. 637262)	40 ±7	4.17
ZnO	Powder	Sigma-Aldrich (Cat. No. 544906)	60 ±20	5.6
ZnO	Powder	Sigma-Aldrich (Cat. No. 205532)	117 ±37	5.6
ZnO	Powder	Sigma-Aldrich (Cat. No. 255750)	144 ±41	5.6
ZnO	Powder	Alfa-Aesar (Cat. No. 44898)	64 ±24	5.6
ZnO	Powder	Alfa-Aesar (Cat. No. 44899)	75 ±33	5.6
ZnO	Powder	Alfa-Aesar (Cat. No. 87812)	155 ±76	5.6
ZnO	Powder	Alfa-Aesar (Cat. No. 11137)	191 ±93	5.6
Fluorescein (acid free)	Powder	Fluka Analytical (Cat. No. 46955)	--	--
Rose Bengal	Powder	Sigma-Aldrich (Cat. No. R3877)	--	--
Rhodamine 6G	Powder	Sigma-Aldrich (Cat. No. R4127)	--	--
Tween 20	Liquid	Sigma-Aldrich (Cat. No. P9416)	--	--
Tween 80	Liquid	Sigma-Aldrich (Cat. No. P1754)	--	--
SDS	Powder	Fisher Scientific (Cat. No. BP166500)	--	--
CTAB	Powder	Sigma-Aldrich (Cat. No. H6269)	--	--
Triton X100	Liquid	MP Biomedicals (Cat. No. 807423)	--	--

Table 2. Summary of kinetic parameters representing ZnO nanoparticles.

	p														
	1			**2**			**3**			**5**			**8**		
d **(nm)**	60	117	144	60	117	144	60	117	144	60	117	144	60	117	144
N **(mol/mol)**	0.137	0.0707	0.0576	0.0436	0.0225	0.0183	0.0269	0.0139	0.0113	0.0161	0.0083	0.0068	0.0103	0.0053	0.0043
R	4.14			4.14			4.05			3.88			3.72		
K **(μM^{-p})**	1.71	1.39	1.15	13.5	8.70	5.77	79.6	37.6	18.6	4,240	794	184	6.19×10^{6}	1.68×10^{5}	7.92×10^{3}
k_{on} **(μM^{-p} s^{-1})**	1.71×10^{-2}	1.39×10^{-2}	1.15×10^{-2}	1.08×10^{-2}	6.96×10^{-3}	4.62×10^{-3}	5.57×10^{-3}	2.63×10^{-3}	1.30×10^{-3}	6.36×10^{-4}	3.57×10^{-4}	1.38×10^{-4}	1.86×10^{-5}	5.04×10^{-6}	2.38×10^{-6}
k_{off} **(s^{-1})**	0.01	0.01	0.01	8×10^{-4}	8×10^{-4}	8×10^{-4}	7×10^{-5}	7×10^{-5}	7×10^{-5}	1.5×10^{-7}	4.5×10^{-7}	7.5×10^{-7}	3×10^{-12}	3×10^{-11}	3×10^{-10}
α ($\times 10^{12}$ m^2/s)	8.04	4.15	3.38	8.04	4.15	3.38	8.04	4.15	3.38	8.04	4.15	3.38	8.04	4.15	3.38

(Summary of kinetic parameter values of p=5, R=3.88 for polydisperse ZnO)

						Sample mean size	
						60	**144**
Size bin (nm)	**Mean size (nm)**	***N*** **(mol/mol)**	***K*** **(μM^{-p})**	k_{on} **(μM^{-p} s^{-1})**	k_{off} **(s^{-1})**	**Particle number %**	**Particle number %**
20-40	30	0.0322	9408	1.64×10^{-3}	1.74×10^{-7}	17.3	0
40-60	50	0.0193	5273	7.59×10^{-4}	1.44×10^{-7}	35.3	0
60-80	70	0.0138	3424	5.82×10^{-4}	1.70×10^{-7}	32.7	3.3
80-100	90	0.0107	2062	5.19×10^{-4}	2.52×10^{-7}	11.3	10.8
100-120	110	0.0088	1060	4.12×10^{-4}	3.89×10^{-7}	2.7	19.2
120-140	130	0.0074	419	2.44×10^{-4}	5.82×10^{-7}	0.7	16.7
140-160	150	0.0064	137	1.14×10^{-4}	8.30×10^{-7}	0	15.8
160-180	170	0.0057	74	8.45×10^{-5}	1.13×10^{-6}	0	15.0
180-200	190	0.0051	51	7.64×10^{-5}	1.49×10^{-6}	0	10.8
200-220	210	0.0046	39	7.43×10^{-5}	1.91×10^{-6}	0	2.5
220-240	230	0.0042	31	7.47×10^{-5}	2.38×10^{-6}	0	4.2
>240	250	0.0039	26	7.65×10^{-5}	2.91×10^{-6}	0	1.7

Table 3. Summary of kinetic parameters representing TiO_2 nanoparticles.

	Anatase TiO_2	Rutile TiO_2
p	1	1
d (nm)	49	40
N (mol/mol)	0.00025	0.004
R	23	0
K (μM^{-1})	1	0.2802
k_{on} ($\mu M^{-1}\ s^{-1}$)	1	0.5604
k_{off} (s^{-1})	1	2
α ($\times 10^{-12}\ m^2/s$)	9.9	12.1

Table 4. Boundary and initial conditions applied in flow model.

Laminar flow boundary condition	
Wall	$\boldsymbol{u} = 0$, $\boldsymbol{n}\cdot\boldsymbol{u} = 0$
Inlet	u = (flow rate) / (cross section area), flow rate = 1.666 e-10 m^3/s
Outlet	$v = 0$, $P = 1$ atm
Transport boundary condition	
Wall	$\boldsymbol{n}\cdot\left(-\alpha\nabla[\mathrm{D}]+[\mathrm{D}]\boldsymbol{u}\right)=0$ $\boldsymbol{n}\cdot\left(-\alpha\nabla[\mathrm{N_S}]+[\mathrm{N_S}]\boldsymbol{u}\right)=0$ $\boldsymbol{n}\cdot\left(-\alpha\nabla[\mathrm{ND}]+[\mathrm{ND}]\boldsymbol{u}\right)=0$
Inlet	$[N_S]$ based on injected suspension concentration and fitted coefficient N $[ND] = 0$ $[D] = 0.005$ mol/m^3
Initial values	
$\boldsymbol{u} = 0$, $P = 1$ atm, $[D] = [N_S] = [ND] = 0$	

Table 5. List of variables and nomenclature.

Variable*	Description
$[N_S]$ (μM)	Available surface binding sites concentration
[D] (μM)	Free dye concentration
[ND] (μM)	Fluorescent complexation concentration
$[M]_i$ (μM)	ZnO concentration calculated by powder mass
p	Bound dye number per surface binding sites
K (μM^{-p})	Equilibrium constant
k_{on} (μM^{-p} s^{-1})	Binding rate constant of dye to surface sites
k_{off} (s^{-1})	Dissociation rate constant of bound dye from surface sites
N (mol/mol)	Coefficient relating ZnO bulk to surface binding sites concentrations
R	Ratio of fluorescence contribution by bound dye to free dye
F_{obs} (a.u.)	Observed fluorescence intensity overall
F'_D (a.u.)	Observed fluorescence intensity by free dye
F'_{ND} (a.u.)	Observed fluorescence intensity by bound dye complexes
F_D (a.u.)	Normalized F'_D
F_{ND} (a.u.)	Normalized F'_{ND}
d (nm)	Nanoparticle diameter
u ($m\ s^{-1}$)	x-dimension (flow direction) velocity
v ($m\ s^{-1}$)	y-dimension (lateral direction) velocity
ρ ($kg\ m^{-3}$)	Density
μ ($kg\ m^{-1}\ s^{-1}$)	Viscosity
α ($m^2\ s^{-1}$)	Diffusion coefficient

* Subscript *i* refers to variables at initial conditions, while *eq* denotes at equilibrium.

Table 6. Nanoparticles grouped by size range for poly disperse model.

Group #	Size bin (nm)	Ave size (nm)	Number%	Mol%
1	20 ~ 40	30	17.3	1.6
2	40 ~ 60	50	35.3	15.0
3	60 ~ 80	70	32.7	38.2
4	80 ~ 100	90	11.3	28.1
5	100 ~ 120	110	2.7	12.1
6	120 ~ 140	130	0.7	5.0

Table 7. Comparison of nonlinear regression between mono disperse and poly disperse models by using of 60 nm ZnO nanoparticles.

Fitted parameters	Mono disperse (average particle size = 60 nm)	Poly disperse	
		Arithmetic average particle size = 60 nm	Cubic average particle size = 66 nm
K	4240	4700	4280
N	0.0161	0.0198	0.0180
R	3.88	3.88	3.88
Sum of squared residuals	295	293	293

Note: p=5, ZnO, tracer=0.5, 1 and 1.5 μM

Table 8. Fitting equation summary

Figure #	Sample	Fitted Equation
15a	Rutile 40 ± 7 nm, batch	y=379.59x+21.18
15a	Anatase 49 ± 9 nm, batch	y=288.24x+16.71
15a	Anatase 137 ± 36 nm, batch	y=80.55x+4.24
15a	Rutile 512 ± 226 nm, batch	y=28.02x+3.18
15b	ZnO 60 ± 20 nm, batch	y=62.02x+9.53
15b	ZnO 117 ± 37 nm, batch	y=8.56x+8.27
15b	ZnO 144 ± 41 nm, batch	y=7.83x+6.26
17a	KCl, Segment Length 17.8 mm	y=0.1446x+0.2879
17a	KCl, Segment Length 8.3 mm	y=0.2072x+0.2093
17b	KCl, Segment Length 16.9 mm	y=0.1598x+0.121
17b	KCl, Segment Length 7.4 mm	y=0.2083x+0.3314
17c	KCl, Segment Length 17.8 mm	y=0.1187x-0.0436
17c	KCl, Segment Length 8.3 mm	y=0.1563x+0.1576
20a	KCl, Segment Length 8.3 mm	y=0.1353x+0.355
16	Anatase 49 ± 9 nm	y=264.31x+48.48
19	TTIP and KCl, batch	$y=3.511x^2-65.56x+316.5$

Table 9. Comparison of nanoparticle characterization methods.

Method name (abbreviation)	Measurement range and medium (limiting factors)	Type of size distribution of raw data	Can deal with challenges of particular types of nanomaeterials? (scale: ++, +, o, -, --)*				Standards for use of method for size analysis available
			Poly-dispersity	Non-spherical particles	Low-density materials	Aggre-gates	
This work	10-200 nm as proved More sensitive to smaller particles	Mean size (extendable with sizer)	-	+	++	++	no
Electron microscopy (EM)	1 nm and higher; dry (dynamic range)	Number-based	+	Long: + Flat: -	-	-	yes
Dynamic light scattering (DLS)	5 nm to 500 nm; suspension (sedimentation, scattering intensity)	(no distribution or scattering-intensity-based)	--	--	+	--	yes
Centrifugal liquid sedimentation (CLS)	20 nm and higher; suspension (particle density)	Extinction-intensity-based	+	--	-	--	yes
Small-angle X-ray scattering (SAXS)	5 nm and higher; suspension (dynamic range)	Scattering-intensity-based	o	-	o	--	yes
Field flow fractionation (FFF)	1 nm to 200 nm; suspension (dynamic range)	(depends on detector)	+	-	+	--	no
Particle tracking analysis (PTA)	25 nm and higher; dry (dynamic range)	Number-based	+	--	o	--	no
Atomic force microscopy (AFM)	1 nm and higher; dry (dynamic range)	Number-based	+	Long: + Flat: +	o	-	yes

*scale: ++ very well, + well, o moderately, - not well, -- not at all